



DEGREE PROJECT IN SPACE TECHNOLOGY,
SECOND CYCLE, 30 CREDITS
STOCKHOLM, SWEDEN 2017

Determination and compensation of magnetic dipole moment in application for a scientific nanosatellite mission

CSABA JÉGER

Determination and compensation of magnetic dipole moment in application for a scientific nanosatellite mission

CSABA JÉGER

Master in Aerospace Engineering

Date: August 20, 2017

Supervisor: Mykola Ivchenko

Examiner: Tomas Karlsson

Swedish title: Fastställande och kompensation för magnetisk
dipolmoment i applikation för vetenskapliga nanosatellituppdrag

School of Electrical Engineering

Abstract

SEAM (Small Explorer for Advanced Missions) is a 3U CubeSat developed at KTH Royal Institute of Technology which will provide high-quality DC and AC magnetic field measurements of Earth's magnetic field. The measurement system requires extended periods of time up to 1000 seconds without active attitude control. The satellite will use passive gravity gradient stabilization and dipole cancellation via a separate set of magnetorquers to satisfy LVLH pointing requirements during the coasting phases. In this thesis a detailed model of satellite magnetic moment is presented which includes dipole moment sources from on-board current loops. The attitude dynamics of the satellite is characterized with simulations and a strategy is proposed to estimate and compensate the time-dependent magnetic dipole moment using the dipole compensation magnetorquers and an offline estimation algorithm. The algorithm is tested with simulated error sources and noise and was found to be able to robustly identify and cancel out the satellite dipole to satisfy mission requirements.

Keywords: cubesat, magnetic dipole estimation, attitude dynamics

Sammanfattning

SEAM (Small Explorer for Advanced Missions) är en 3U CubeSat utvecklad på KTH Kungliga tekniska högskolan för DC och AC magnetiskfältsmätningar av Jordens magnetfält. Mätningar kräver längre tidperioder upp till 1000 sekunder utan aktiv attitydstyrning. Satelliten kommer använda passiv tyngdkraftsgradientstabilisering samt magnetisk dipolmomentkompensation med hjälp av ett separat set av magnetiska spolar för att upprätthålla orienteringskrav under perioder utan attitydstyrning. Denna rapport presenterar en detaljerad modell av satellitens magnetiskt dipolmoment som inkluderar dipolmomentkällor från strömslingor ombord satelliten. Satellitens attityddynamik är karakteriserad med simulationer och en strategi tas fram för att estimeras och kompensera det tidsberoende magnetiska dipolmomentet genom att använda dipolkompensations magnetiska spolar och en offline estimeringsalgoritm. Algoritmen är testad med simulerade felkällor och brus och har funnits pålitlig för uppskattning av dipolmomentet och dess kompensation för att uppfylla missionskrav.

Nyckelord: cubesat, magnetisk dipol uppskattning, attityddynamik

Acknowledgements

I would like to express my gratitude first and foremost to Dr. Nickolay Ivchenko for the opportunity to work on the SEAM project and for his supervision and help during this work. I would also like to thank Dr. Gunnar Tibert and Sven Grahm for guiding and inspiring me during my master's years and for all the immensely valuable lessons I would not have learned without them on not just satellite dynamics but the space industry in general.

I would not be here without my parents, Tibor Jéger and Judit Sze-merády who always believed in me and helped me achieve everything I aimed for.

Special thanks for my fellow student Gustav Pettersson for his extremely valuable help in solar cell modelling and Malte Gruber for practical matters of the satellite.

Last but not least I would like to thank all my friends who I had the honor to share the last two years, especially Niels Bernving and Periklis-Konstantinos Diamantidis, both of whom I have spent many long working hours at KTH.

Contents

Contents	vi
1 Introduction	1
1.1 The CubeSat standard	1
1.2 The SEAM project	2
1.2.1 Science instruments	3
1.2.2 ADCS requirements	5
1.2.3 Attitude Determination and Control System . . .	6
1.2.4 Magnetic dipole compensation	7
1.3 Master thesis aim	7
2 Attitude Dynamics	9
2.1 Attitude Representations	9
2.1.1 Direction Cosine Matrix	9
2.1.2 Principal Rotation Vector	11
2.1.3 Euler angles	12
2.1.4 Quaternions	13
2.2 Two Line Elements (TLE)	14
2.3 Coordinate systems	15
2.3.1 Earth-Centered Inertial (ECI)	16
2.3.2 Earth-Centered Earth-Fixed (ECEF)	16
2.3.3 Latitude Longitude Altitude (LLA)	17
2.3.4 Orbital Coordinate Frame (OCF)	18
2.3.5 Body-fixed	19
2.4 Equations of motion	20
2.5 Disturbance Torques	21
2.5.1 Magnetic torque	22
2.5.2 Gravity gradient torque	23
2.5.3 Atmospheric drag torque	24

2.5.4	Radiation pressure torque	26
3	Magnetic Dipole Modelling	29
3.1	Magnetic Dipole Sources	29
3.2	Power system	30
3.3	Solar cell model	31
3.4	Magnetic dipole compensation	32
3.4.1	Compensation Algorithm	33
3.4.2	Model limitations	34
4	Implementation	35
4.1	Simulation setup	35
4.1.1	Satellite	36
4.1.2	Environment	37
4.1.3	Pointing	38
4.2	Results	39
4.2.1	Forward model without compensation	39
4.2.2	RMD estimation	41
4.2.3	Forward model with compensation	44
4.2.4	RMD estimation with albedo disturbances and sensor noise	45
4.3	Simulation errors	47
5	Conclusion	50
5.1	Estimation	50
5.2	Compensation	51
5.3	Further work	51
	Bibliography	52

Chapter 1

Introduction

Satellites were traditionally large, heavy and extremely expensive pieces of hardware, reserved for the biggest-budget governmental agencies and companies. This status quo was challenged and disrupted in recent years with the rise of a new type of private space industry, with the need for fast, cheap and innovative access to space-based infrastructure. The flagship of this progress is the cubesat spacecraft. Cubesats are a special, standardized class of nanosatellites gaining enormous popularity in the past decade. This is mainly due to the low-cost, COTS-reliant approach to satellite design which is made possible by the ever-increasing available computational power and miniaturization efforts. We will start this chapter with a general description of cubesats, then detail the subject satellite of this work, the SEAM project. We will close the chapter with the scope and goals of this MSc thesis.

1.1 The CubeSat standard

Originally developed in 1999 at California Polytechnic State University and Stanford University for student space projects, the CubeSat standard specifies a type of nanosatellite made up of 10x10x10 cm cube units, weighting no more than 1.33 kg per unit. The standard provides a well-defined interface between the launcher and the satellite, which makes the launch qualification of these satellites uniform and streamlined. The standard is specified and updated regularly in the CubeSat design specification document [1]. Currently by far the most popular format is the 3-unit (denoted 3U) cubesats which provide a good trade-

off between capabilities and cost with over 50 percent of all cubesats in orbit being 3U [2].

Cubesats are usually launched from auxiliary payload adapters mounted on larger launch vehicles or from the International Space Station (in the beginning, by actually throwing it by hand, lately from dedicated deployers). The deployment mechanism used on launch vehicles is also standardized and is called the Poly Picosat Orbital Deployer (P-POD) which is a spring-loaded mechanism in an aluminum container carrying at least 3 units. During ascent, the launch vehicle deploys the contents of the P-POD along the destination of its primary payload by opening the container hatch. A P-POD container is illustrated on 1.1.

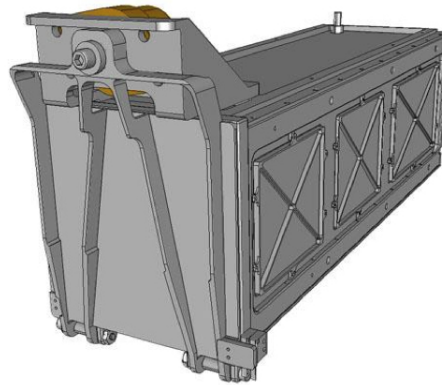


Figure 1.1: A 3U Poly Picosat Orbital Deployer (P-POD) design [1].

The outer dimensions and protrusions of the satellite are tightly controlled by the standard thus any deployable structure (solar panels, antennae, booms) have to be stowed until after separation. The satellite is completely powered off during launch to prevent any interference with the launch vehicle. While stowed in the deployer, a redundant pair of spring-loaded kill switches keep the satellite off. As the satellite is released, the switches pop out, turning the satellite on.

1.2 The SEAM project

The Small Explorer for Advanced Missions (SEAM) is a collaboration project in the Framework Programme 7 of the European Union. The project is lead by KTH Royal Institute of Technology and aims to provide high-quality three-axis DC and AC magnetic field measurements

of Earth's magnetic field. The scientific aim of the satellite is to help characterize auroral currents and investigate ELF/VLF emissions from natural and man-made sources using two sets of magnetometers. The satellite is designed to operate in a high-inclination Low-Earth Orbit (LEO) for a design lifetime of 1 year and is scheduled to launch in December 2017.

The satellite features magnetic control with passive gravity gradient stabilization which are achieved using booms which also house the two science instruments. There are two deployable solar panels mounted on the satellite which deploy at 135 degrees angle for added aerodynamic stability. The partially-deployed satellite can be seen on Figure 1.2 with the booms stowed in the satellite body.

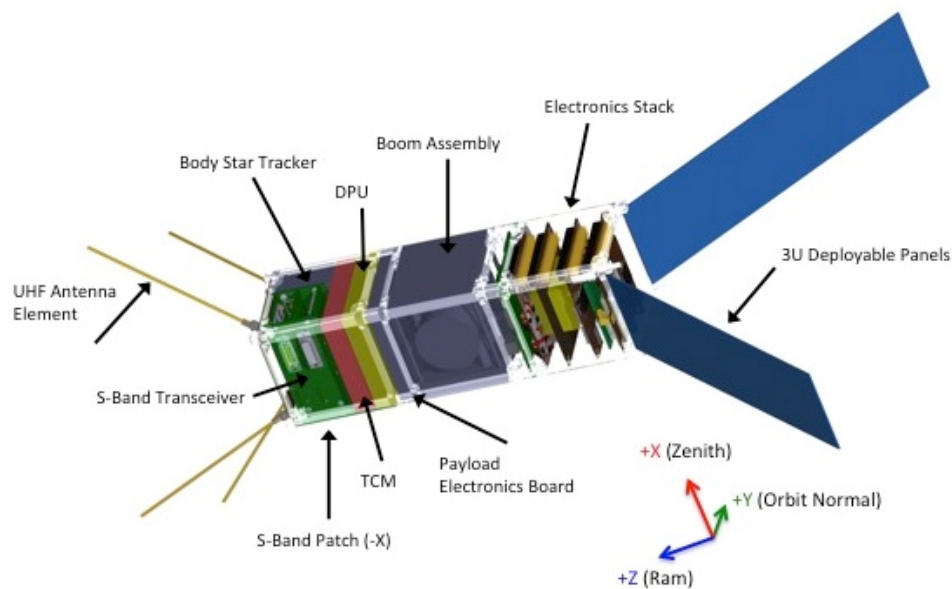


Figure 1.2: The SEAM satellite without the boom assembly deployed.

1.2.1 Science instruments

The two magnetometers have to provide high spatial and temporal resolution magnetic field data while being constrained by the small size and available power of the satellite. To minimize interference from the satellite, both sensors are mounted on deployable booms extending from the middle unit.

SMILE flux-gate magnetometer

SMILE is an extremely compact high sensitivity fluxgate sensor capable of measuring all three components of DC and low-frequency magnetic field. The sensor itself is only 0.20x0.20x0.21 cm weighting 20 grams and was developed jointly by KTH Royal Institute of Technology and Lviv Centre of Institute of Space Research (LEMI) [3] and can be seen on Figure 1.3.

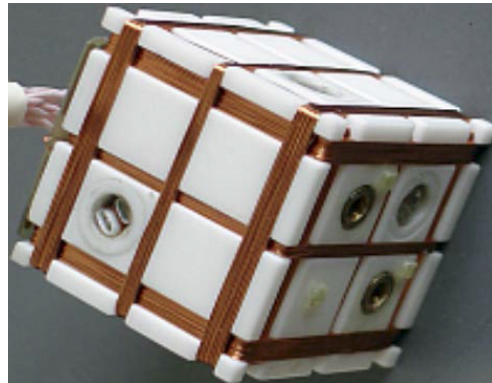


Figure 1.3: The SMILE magnetometer sensor.

Search coil magnetometer

The LEMI-151 search-coil (or induction) magnetometer is intended to measure three components of AC magnetic field. It was specifically developed for the SEAM mission to achieve high performance while having a low volume. The magnetometer can be seen on Figure 1.4.

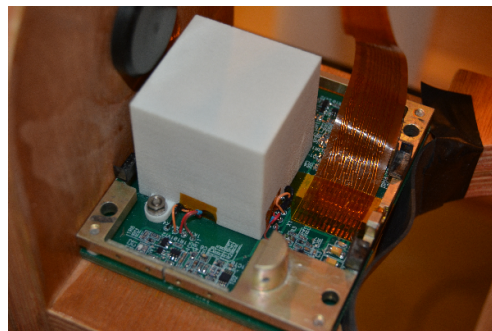


Figure 1.4: The search coil magnetometer on its PCB unit.

1.2.2 ADCS requirements

The mission goals put tight requirements on the Attitude Determination and Control System (ADCS). The ADCS-relevant requirements are summarized in Table 1.1. The challenge here arises from two requirements. First, the primary magnetic control system interferes with the scientific instruments so it must be powered off during observation periods for up to 1000 seconds. Second, the satellite should be stabilized within 10 degrees of the Local Vertical Local Horizontal (LVLH) system. The combination of these two requirements means that the satellite requires static stabilizing components.

Requirement	Definition
2.SYS.FR.14	Attitude knowledge of the fluxgate sensor is required within 1 arcminute
2.SYS.FR.15	The satellite attitude shall be stabilized to within 10 degrees of the local vertical local horizontal system
2.SYS.FR.16	Active attitude corrections disturbing the scientific measurements shall on average have a duty cycle of under 10%
2.SYS.FR.17	Satellite should allow periods of up to 1000 seconds without activating the magnetic torquers.
2.SYS.MC.2	Attitude control shall be a combination of gradient gravity passive control and active corrections by means of magnetic torquers
2.SYS.MC.7	The satellite shall have a system of two deployable booms, providing gravity gradient stabilization and keeping the science sensors away from the satellite body.
2.SYS.MC.8	Controllable current sources may be used with magnetic torquers to compensate the residual magnetic moment of the satellite to within 0.1 mAm^2 on each axis.

Table 1.1: ADCS-related system requirements for SEAM.

1.2.3 Attitude Determination and Control System

SEAM has two physically identical computers from which one is dedicated for running the ADCS loop. The satellite also uses a number of different sensors and actuators to determine and control its attitude. Figure 1.5 shows the subsystem components in color. The on-board sensors are the following:

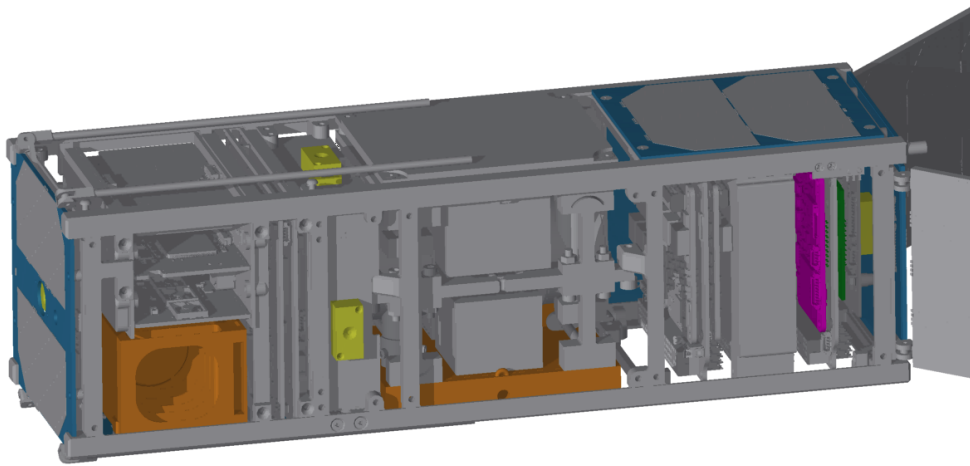


Figure 1.5: SEAM with wings deployed; ADCS sensors and actuators highlighted. Note that some panels were removed for clarity.

- Coarse sun sensors integrated in all solar cells (not colored)
- 6 fine sun sensors on all sides of the satellite structure (yellow)
- Boom star tracker on the top boom (orange)
- Body-mounted star tracker, located in the first unit (orange)
- Integrated 3-axis magnetometers, located on the OBC and the ADCS computers (purple)
- Integrated 3-axis gyroscope, located on the OBC and the ADCS computers (purple)

There are two sets of magnetic actuators on the satellite:

- 3-axis magnetorquer in the ADCS stack (purple)
- 3-axis magnetic bias coils, integrated in special solar panels (teal)

1.2.4 Magnetic dipole compensation

It has been discussed earlier that there are strict requirements on satellite pointing even when the ADCS is not running. The magnetic torque experienced by the satellite is caused by the interaction of the magnetic field of Earth and SEAM, which generates a dipole field characterized with the magnetic dipole moment. In case of cubesats, the largest source of disturbance is usually the magnetic. This is because magnetic torque scales linearly with mass while other disturbance torques scale linearly with the projected area which in turn roughly scales with the square of the mass, thus magnetic disturbance torques become dominant quickly as the size of the satellite gets smaller.

There are two strategies for reducing the magnetic moment; ensuring that the satellite is constructed from magnetically clean materials or using passive or active magnetic components to negate the dipole moment. For cubesats, dipole moment is often left to be handled by ADCS since stricter cleanliness requirements cause the costs to rise sharply, which works against the cubesat design philosophy of cost minimization.

In case of SEAM the second set of magnetorquers is used to compensate the magnetic dipole moment of the satellite and provide an in-flight calibration signal for the search-coil magnetometer. It is operated from an OBC-controllable current source and is capable of generating 34 to 43 mAm^2 dipole moment (temperature dependent) with an effective area of 1.55 m^2 .

1.3 Master thesis aim

The objective of the MSc thesis work is to develop strategies for in-orbit estimation of the static and variable magnetic moments, and algorithms for their compensation. The tasks in the thesis include:

- Getting familiar with the SEAM satellite on the system level, including operation modes, telemetry/telecommand, operation and handling of the satellite.

- Getting familiar with the ADCS system of the SEAM satellite, including the sensors, and actuators, testing the function and performance of the sensors, and interpretation of their measurements.
- Participating in magnetic characterization of the satellite in order to estimate its magnetic dipole moment.
- Creating a model of the satellite attitude dynamics.
- Proposing a strategy for estimating the magnetic dipole moment vector from attitude dynamics behaviour of the satellite.
- Developing an algorithm for time-dependent control of the magnetic dipole compensation currents to be implemented in orbit.

Chapter 2

Attitude Dynamics

This chapter describes the problem of attitude determination in the context of modeling and reconstructing attitude information from sensor data. First, we will discuss the coordinate systems and attitude representations used, then the theoretical background and disturbance models.

2.1 Attitude Representations

There are several ways to describe a given orientation in a reference frame described later in Section 2.3. In this work, several attitude representations are used depending on the application area. In this section we will briefly review these and their relation to each other [4]. In all cases it will be assumed that the reference frames considered have the same origin and thus no translation of the frames is required.

2.1.1 Direction Cosine Matrix

The most fundamental way of describing the orientation of two frames relative to each other is to describe their basis vectors in the other frame. In \mathbf{R}^3 Let two reference frames \mathcal{N} and \mathcal{B} be defined with three orthonormal base vectors $\hat{\mathbf{n}}_{1,2,3}$ and $\hat{\mathbf{b}}_{1,2,3}$ which are illustrated on Figure 2.1. The angle α_{ij} between a particular base vector $\hat{\mathbf{b}}_i$ and a base vector from the \mathcal{N} frame $\hat{\mathbf{n}}_j$ is called a direction cosine. Using the direction cosines we can express $\hat{\mathbf{b}}_i$ in terms of the base vectors $\hat{\mathbf{n}}_{1,2,3}$ as:

$$\hat{\mathbf{b}}_i = \cos \alpha_{i1} \hat{\mathbf{n}}_1 + \cos \alpha_{i2} \hat{\mathbf{n}}_2 + \cos \alpha_{i3} \hat{\mathbf{n}}_3 \quad (2.1)$$

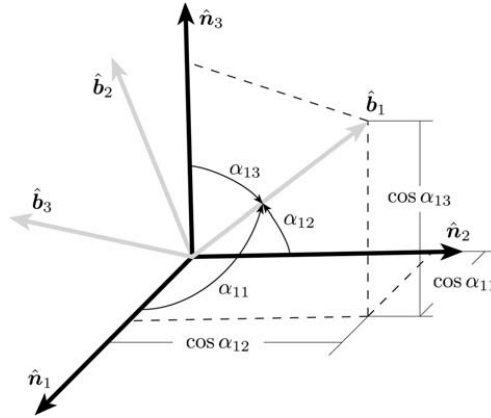


Figure 2.1: Definition of the direction cosines [4].

We can use Eq. 2.1 to define a compact transformation between the base vectors by constructing a 3-by-3 matrix of the direction cosines. A more useful property is the ability to transform arbitrary vectors from one frame to another, which can be easily shown from Eq. 2.1. An arbitrary vector \mathbf{v} in the \mathcal{N} frame can be expressed in the \mathcal{B} frame using the newly-defined Direction Cosine Matrix (DCM) $[C]_{bn}$ as:

$$\mathbf{v}_b = \begin{bmatrix} \cos \alpha_{11} & \cos \alpha_{12} & \cos \alpha_{13} \\ \cos \alpha_{21} & \cos \alpha_{22} & \cos \alpha_{23} \\ \cos \alpha_{31} & \cos \alpha_{32} & \cos \alpha_{33} \end{bmatrix} \mathbf{v}_n = [C]_{bn} \mathbf{v}_n \quad (2.2)$$

Due to the definition of its elements, this matrix has extremely useful properties which make it an essential tool in attitude modelling. The inverse of the matrix describes rotation between the frames in the other direction:

$$[C]_{bn}^{-1} = [C]_{nb} \quad (2.3)$$

Matrix inversion is a computationally costly operation but fortunately, it can be shown that the DCM is orthogonal, thus its inverse equals its transpose, which in turn is a fast operation:

$$[C]_{bn}^{-1} = [C]_{bn}^T \quad (2.4)$$

The DCM also has a composition property, which means that successive rotations can be described as matrix multiplications of individual matrices:

$$[C]_{rn} = [C]_{bn} [C]_{rb} \quad (2.5)$$

DCMs are a powerful tool to naturally describe attitude. However, using 9 parameters to describe orientation is highly redundant. Moreover, just by looking at the matrix the orientation cannot be intuitively determined. Despite this, DCMs are still widely used due to the previously described attractive properties. We will also use DCMs to define and relate other, more compact attitude representation to each other.

2.1.2 Principal Rotation Vector

This attitude description builds on Euler's rotation theorem, which states that any coordinate system in \mathbf{R}^3 can be brought to an arbitrary orientation using a single rotation Φ around some axis which we will call the principal axis \hat{e} which is illustrated on Fig. 2.2. It is customary to combine these two into a single vector called the Principal Rotation Vector (PRV) as:

$$\mathbf{r} = \Phi \hat{e} \quad (2.6)$$

Due to this definition, inverting the sign of both Φ and \hat{e} will result in the same PRV and correspond to the same orientation. Moreover, the rotation angle is not unique either as rotating by $\Phi' = \Phi - 360$ i.e. in the other direction will achieve the same result. In this work the notation will be that Φ corresponds to the shorter ($> 180 \text{ deg}$) rotation.

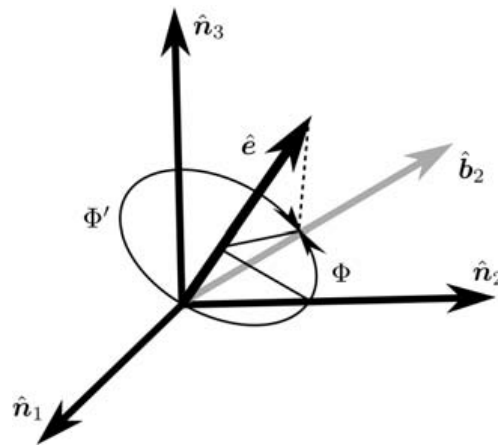


Figure 2.2: Definition of the principal rotation vector. [4].

The Principal Rotation Vector can be converted to a DCM with the

following relation:

$$[C] = \begin{bmatrix} e_1^2 \Sigma + \cos \Phi & e_1 e_2 \Sigma + e_3 \sin \Phi & e_1 e_3 \Sigma - e_2 \sin \Phi \\ e_2 e_1 \Sigma - e_3 \sin \Phi & e_2^2 \Sigma + \cos \Phi & e_2 e_3 \Sigma + e_1 \sin \Phi \\ e_3 e_1 \Sigma + e_2 \sin \Phi & e_3 e_2 \Sigma - e_1 \sin \Phi & e_3^2 \Sigma + \cos \Phi \end{bmatrix} \quad (2.7)$$

Here $\Sigma = 1 - \cos \Phi$ and $e_{1..3}$ are the components of the eigenrotation vector. In the other direction, the Principal Rotation Vector can be constructed as:

$$\cos \Phi = \frac{1}{2} (C_{11} + C_{22} + C_{33} - 1) \quad (2.8)$$

$$\hat{\mathbf{e}} = \begin{pmatrix} e_1 \\ e_2 \\ e_3 \end{pmatrix} = \frac{1}{2 \sin \Phi} \begin{pmatrix} C_{23} - C_{32} \\ C_{31} - C_{13} \\ C_{12} - C_{21} \end{pmatrix} \quad (2.9)$$

2.1.3 Euler angles

Euler angles describe attitude of a rigid body as a sequence of three rotations around the axes of a fixed coordinate system. If the coordinate system is fixed to some resting frame the rotation sequence is said to be extrinsic, if it is fixed to the rigid body, it is called an intrinsic rotation sequence. In aerospace applications intrinsic sequences are used as rate sensors are fixed to the body frame which correspond to the definition of intrinsic rotations so from now on we will only consider these. There are 12 ways to define these three rotations and depending on whether rotation through the same axes is allowed or not they can be split to two categories. In the former case where all three axes are used, these rotations are called Tait-Bryan angles, the latter one is referred as Proper Euler angles. However, in this text we will refer to the z-y-x or yaw-pitch-roll (ϕ, θ, ψ) Tait-Bryan angle sequence as *the* Euler angles of the spacecraft body frame, illustrated on Fig. 2.3.

Euler angles are popular due to their intuitiveness for small angles and relatively compact form thus they are widely used to visualize attitude. Unfortunately it can be easily proven that not only the rotations are not unique for either of the axis combinations but they also contain singularities. This is related to the physical phenomenon called gimbal lock in mechanical gyroscopes.

The DCM for a given Euler angle sequence can be easily constructed by using the composition property (2.2) and multiplying the elementary rotation matrices for each Euler angle:

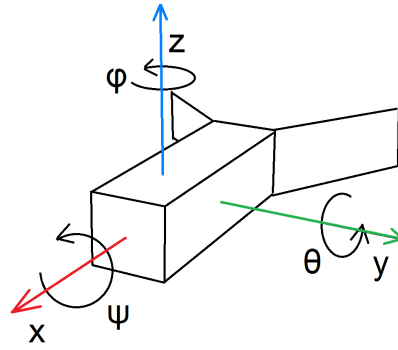


Figure 2.3: Euler angles of the satellite, tied to the body frame.

$$[R_x] = \begin{bmatrix} 1 & 0 & 0 \\ 0 & \cos \psi & -\sin \psi \\ 0 & \sin \psi & \cos \psi \end{bmatrix} \quad (2.10)$$

$$[R_y] = \begin{bmatrix} \cos \theta & 0 & \sin \theta \\ 0 & 1 & 0 \\ -\sin \theta & 0 & \cos \theta \end{bmatrix} \quad (2.11)$$

$$[R_z] = \begin{bmatrix} \cos \phi & -\sin \phi & 0 \\ \sin \phi & \cos \phi & 0 \\ 0 & 0 & 1 \end{bmatrix} \quad (2.12)$$

$$[C] = [R_x][R_y][R_z] = \begin{bmatrix} c\theta c\psi & c\theta s\psi & -s\theta \\ s\phi s\theta c\psi - c\phi s\psi & s\phi s\theta s\psi + c\phi c\psi & s\phi c\theta \\ c\phi s\theta c\psi + s\phi s\psi & c\phi s\theta s\psi - s\phi c\psi & c\phi c\theta \end{bmatrix} \quad (2.13)$$

where c and s correspond to \cos and \sin respectively.

2.1.4 Quaternions

Also called Euler parameters, quaternions are a powerful, redundant attitude description. Attitude is described as a 4-dimensional unit vector and rotations are trajectories between two 4-vectors on the surface of a hypersphere. In general, quaternions are hypercomplex numbers in the form $a + bi + cj + dk$ [5]. The first term a is called the scalar part

and the rest is the vector part. In this work we employ the following notation where 0 denotes the scalar part:

$$\mathbf{q} = \begin{bmatrix} q_0 & q_1 & q_2 & q_3 \end{bmatrix} \quad (2.14)$$

We define quaternions using the Principal Rotation Vector elements described in Section 2.1.2:

$$q_0 = \cos(\Phi/2) \quad (2.15a)$$

$$q_1 = e_1 \sin(\Phi/2) \quad (2.15b)$$

$$q_2 = e_2 \sin(\Phi/2) \quad (2.15c)$$

$$q_3 = e_3 \sin(\Phi/2) \quad (2.15d)$$

The non-uniqueness from principal rotations will be present here as well and it can be shown that the vector $-\mathbf{q}$ describes the same attitude as \mathbf{q} . It can be also seen from Eq. 2.15 that the resulting quaternion will be an unit vector as \hat{e} is an unit vector by definition. This means that \mathbf{q} satisfies the following relation:

$$q_0^2 + q_1^2 + q_2^2 + q_3^2 = 1 \quad (2.16)$$

While working with quaternions it is important to ensure the condition in Eq. 2.16 as numeric errors will keep accumulating which is a source of numerical error. The solution is to periodically normalize the attitude quaternion during calculation. Quaternions are a popular choice for satellite attitude modeling as they do not suffer from singularities and are computationally very efficient, offering a good trade-off between DCMs and Euler angles.

2.2 Two Line Elements (TLE)

A Two-Line Element set is a format developed by NORAD in the 1950s to describe the orbit of Earth-orbiting satellites as part of the SGP4/SDP4 orbital model (propagator) [6]. Today NORAD tracks satellites and space debris in orbit and orbital information is available in the TLE format. A TLE set consists of two lines of 69 characters plus an optional header line. The orbit propagators are empirical and output velocity and position coordinates with kilometer units in an inertial frame. This will be discussed in more detail in Section 2.3. The accuracy of TLEs is believed to be approximately 1 km at epoch, growing at about 1 to 2 km per day so they need to be updated frequently to keep track of objects in orbit [7]. The reference TLE of the SEAM satellite is:

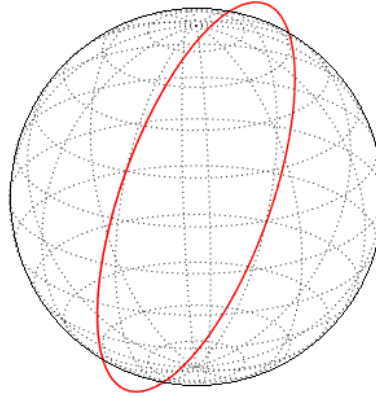


Figure 2.4: Reference orbit visualized from the TLE in the inertial frame.

```
SEAM
1 00032U 16624A 17001.00000000 +.00000000 +00000-0 +00000-0 0 00010
2 00032 97.9770 057.6960 0030000 090.0000 000.0000 14.91626772000000
```

which corresponds to a semi-major axis of 6970 km (600 km altitude) orbit with an inclination of 98 degrees. The full description of the format follows the TLE documentation [6]. The plotted orbit from the reference TLE can be seen on Fig. 2.4.

2.3 Coordinate systems

In astronautics and astronomy, the general problem of describing the position, orientation and dynamics of an object requires the use of several different coordinate systems (frames). The orientation of these frames with respect to each other is usually not constant and is typically defined using a date-reference (epoch). For satellite attitude description, it is typical to use at least an inertial and a satellite body-fixed frame. It is important to note that multiple slightly or significantly different frames and reference systems exist to fulfill the previously mentioned roles. While modeling small disturbances such as in this work, one must be aware of the slight differences to avoid introducing unwanted errors into the computations.

2.3.1 Earth-Centered Inertial (ECI)

To describe the dynamics we will need an inertial frame of reference. The chosen frame of reference is in the family of Cartesian Earth-Centered Inertial (ECI) systems. This ECI coordinate system is defined by the International Astronomical Union and is called the Geocentric Celestial Reference Frame (GCRF) [8]. The GCRF axes are oriented according to the International Celestial Reference Frame (ICRF) axes, thus there is only a time-independent translation transform between them. The epoch used for the systems is called J2000.0 and refers to 12pm (noon) GMT 2000.01.01 according to the Gregorian calendar. The ICRF axes are determined and maintained from careful observations of distant quasars but their direction was chosen to be close to the following definition at the J2000.0 epoch:

- The coordinate system origin is at the center of mass of Earth
- x-axis: pointing towards the vernal equinox
- z-axis: pointing towards the rotation axis of the Earth
- y-axis: completes the right-hand set

It is noted here that TLE propagation is done in the True Equator Mean Equinox (TEME) frame, which is different from the GCRF frame. The exact definition of the TEME frame used in the propagation models is hard to find but the agreed method to link the TEME frame to GCRF is via the following process: from TEME, convert to Time of Day (TOD) using the IAU 1996 conventions without corrections, then to Mean Equator of Date (MOD) also using the IAU 1996 conventions without corrections, then to GCRF. However, the position difference between the two frames is below 2.5 meters [9] thus it will be disregarded for the purposes of this work.

2.3.2 Earth-Centered Earth-Fixed (ECEF)

Earth-Centered Earth-Fixed (ECEF) axes are required to calculate magnetic and atmospheric disturbance as well as Earth albedo parameters as these sources of disturbance rotate with the Earth. The main ECEF frame used in this work is the International Terrestrial Reference Frame (ITRF) which takes into account nutation and precession and its model is updated from measurements regularly. Another common

ECEF definition is the WGS84 frame, which is used in some coordinate transformations and notably is the system used by GPS. The difference between the ITRF and WGS84 is being maintained to be less than one meter and thus they will be assumed identical [10]. The epoch used is also J2000.0 for both frames.

- The coordinate system origin is at the center of mass of Earth
- x-axis: pointing towards the prime meridian
- z-axis: pointing towards the rotation axis of the Earth
- y-axis: completes the right-hand set

During conversion from ECI to ECEF, the x and y axes are rotated depending on the current time, and then the result is adjusted for nutation, precession and polar motion. Implementation of the transform is done using the MATLAB function `dcmeci2ecef`.

2.3.3 Latitude Longitude Altitude (LLA)

This is a spherical coordinate frame with the usual definition of geographic latitude, longitude and altitude on a reference geoid, illustrated on Fig. 2.5, In this case, the geoid defined by the WGS84 frame is used which has the following ellipsoid parameters:

a	6378137 m
$1/f$	298.257224

Table 2.1: WGS84 ellipsoid parameters [10].

In Table 2.1 the parameter a is the semi-major axis and f is the flattening. The relationship between the ECEF and LLA frames is then given by the following relation:

$$\mathbf{r}_{\text{ECEF}} = [x \ y \ z] \quad \mathbf{l}\mathbf{a} = [\phi \ \lambda \ h] \quad (2.17)$$

$$\begin{aligned} x_{\text{ECEF}} &= (aC + h) \cos(\phi) \cos(\lambda) \\ y_{\text{ECEF}} &= (aC + h) \cos(\phi) \sin(\lambda) \\ z_{\text{ECEF}} &= (aS + h) \sin(\phi) \end{aligned} \quad (2.18)$$

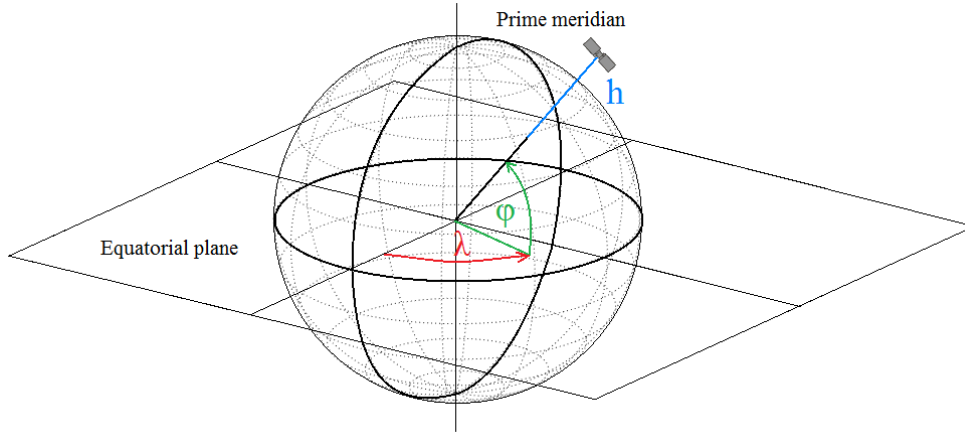


Figure 2.5: Definition of the Latitude Longitude Altitude frame.

$$C = \frac{1}{(\cos^2 \phi + (1 - f)^2 \sin^2 \phi)^{1/2}} \quad (2.19)$$

$$S = (1 - f)^2 C \quad (2.20)$$

2.3.4 Orbital Coordinate Frame (OCF)

This is a Cartesian coordinate frame is a rotating local horizontal frame used to define the pointing of the satellite and calculate atmospheric drag forces and solar pressure. The frame is defined as:

- The coordinate system origin is at the center of mass of the satellite
- x-axis: pointing towards the orbital velocity vector
- z-axis: parallel with the position vector
- y-axis: completes the right-hand set

The frame is also illustrated on Fig. 2.6. Note that this definition is not the most frequently used, where the $+z$ axis points toward nadir. The transformation from the ECI to the OCF frame involves translation and rotation. When needed, the translation is straightforward along the position vector of the satellite. The DCM of the rotation can be

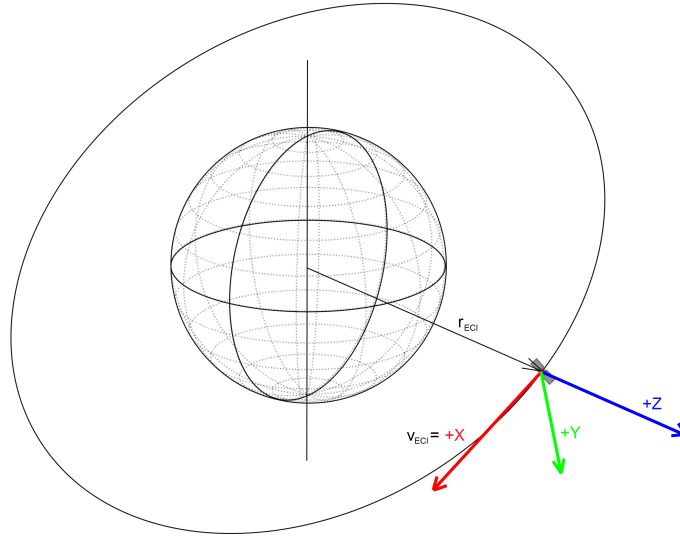


Figure 2.6: Definition of the Orbital Coordinate Frame.

obtained from the position and velocity vector using the definition of the frame and using Eq. 2.1-2.2:

$$\begin{aligned}\hat{\mathbf{z}}_{OCF} &= \frac{\mathbf{r}_{ECI}}{|\mathbf{r}_{ECI}|} \\ \hat{\mathbf{y}}_{OCF} &= \frac{\mathbf{r}_{ECI} \times \mathbf{v}_{ECI}}{|\mathbf{r}_{ECI} \times \mathbf{v}_{ECI}|} \\ \hat{\mathbf{x}}_{OCF} &= \frac{\mathbf{y}_{OCF} \times \mathbf{z}_{OCF}}{|\mathbf{y}_{OCF} \times \mathbf{z}_{OCF}|}\end{aligned}\tag{2.21}$$

$$[C]_{ECI,OCF} = \begin{bmatrix} \hat{\mathbf{x}}'_{OCF} \\ \hat{\mathbf{y}}'_{OCF} \\ \hat{\mathbf{z}}'_{OCF} \end{bmatrix}\tag{2.22}$$

2.3.5 Body-fixed

The body-fixed frame is used to define the Euler angles and the inertia tensor of the satellite. Note that this frame is a right-hand set different from the CAD coordinate system defined in the assembly file. In this definition when the satellite is in nominal orientation (i.e. zero pointing error) the Body frame coincides with the OCF. The coordinate system is illustrated on Fig. 2.7. The frame is defined as:

- The coordinate system origin is at the center of mass of the satellite

- x-axis: pointing towards the ram direction
- z-axis: pointing towards the boom containing the star tracker.
- y-axis: completes the right-hand set

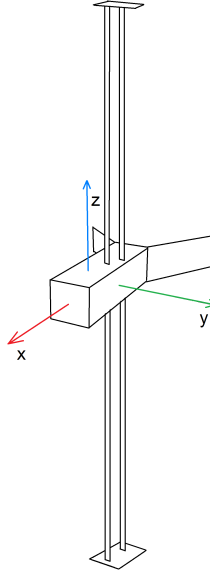


Figure 2.7: Definition of the body frame.

The transformation of this frame is described by the attitude quaternion itself. It can be written as a DCM in the following form:

$$[C]_{ECI,b} = \begin{bmatrix} q_1^2 + q_2^2 - q_3^2 - q_4^2 & 2(q_2q_3 + q_1q_4) & 2(q_2q_4 - q_1q_3) \\ 2(q_2q_3 - q_1q_4) & q_1^2 - q_2^2 + q_3^2 - q_4^2 & 2(q_3q_4 + q_1q_2) \\ 2(q_2q_4 + q_1q_3) & 2(q_3q_4 - q_1q_2) & q_1^2 - q_2^2 - q_3^2 + q_4^2 \end{bmatrix} \quad (2.23)$$

2.4 Equations of motion

The equations of motion used in this work assume that the satellite is a rigid body and we can write the conservation of angular momentum in the usual form for the whole spacecraft:

$$\dot{\mathbf{H}}_{in} = I\dot{\boldsymbol{\omega}}_{in} = \mathbf{T}_{in} \quad (2.24)$$

In the Eq. 2.24, \mathbf{H} is the angular momentum vector, I is the inertia tensor of the rigid body in the inertial coordinate frame and $\boldsymbol{\omega}$ is the angular velocity vector. The term \mathbf{T} is the torque vector acting on the satellite, including both the disturbances and control system. Instead of this form, the equation is usually solved in the body frame due to the inertia matrix being constant there. Note that from now on the indices are dropped for the body frame. Using the transport theorem Equation 2.24 takes the following form in the body frame:

$$I\dot{\boldsymbol{\omega}} + \boldsymbol{\omega} \times I\boldsymbol{\omega} = \mathbf{T} \quad (2.25)$$

To complete the equation system we establish the relation between the attitude quaternion and the angular velocity vector using the formula derived in [4]:

$$\begin{pmatrix} \dot{q}_0 \\ \dot{q}_1 \\ \dot{q}_2 \\ \dot{q}_3 \end{pmatrix} = \frac{1}{2} \begin{bmatrix} 0 & -\omega_1 & -\omega_2 & -\omega_3 \\ \omega_1 & 0 & \omega_3 & -\omega_2 \\ \omega_2 & -\omega_3 & 0 & \omega_1 \\ \omega_3 & \omega_2 & -\omega_1 & 0 \end{bmatrix} \begin{pmatrix} q_0 \\ q_1 \\ q_2 \\ q_3 \end{pmatrix} \quad (2.26)$$

Together Equation 2.25 and 2.26 describe the complete system dynamics. Because of this, they are solved together using the system state vector $\mathbf{x} = [\mathbf{q} \ \boldsymbol{\omega}]$. In the next section we will define the torques acting on the spacecraft.

2.5 Disturbance Torques

Empty space is a perfectly torque-free environment. Unfortunately, space is never completely empty, especially not in Low-Earth Orbit thus satellites and spacecraft have to deal with disturbances. These apply forces and torques to the objects altering their trajectory and attitude. In this work, attitude dynamics is decoupled from orbital mechanics, the latter solved using the SGP4 propagation model discussed earlier in Section 2.2 thus we only need to consider the torques produced. These torques will be very small, ranging from 10^{-5} .. 10^{-9} Nm coming from different sources. The disturbance sources considered here are Earth's magnetic field, gravity, atmosphere and solar radiation. There are some other sources such as micrometeorites and third-body gravitational effects but these are stochastic or small enough to be disregarded in this work.

2.5.1 Magnetic torque

The magnetic field of Earth is causing the largest unwanted torque on SEAM through interaction with the residual dipole of the satellite and is the main focus of the present work. We have already discussed the effects and implications of residual dipole previously. The total torque in some reference frame is calculated as:

$$\mathbf{T}_{mag} = \boldsymbol{\mu} \times \mathbf{B} \quad (2.27)$$

Given the dipole moment μ , the other component in the equation is the magnetic field vector \mathbf{B} . In this section we will address the magnetic field model used. There are several approaches on how to model the magnetic field of our planet. The simplest one is to approximate it with a dipole field, which is enough for certain calculations but disregards the time-varying nature and local deviations of the magnetic field. In this case we will employ a much higher accuracy empirical model which is a spherical harmonic representation using measurements from satellites and ground based stations. Spherical harmonic functions is a mathematical tool used to represent arbitrary functions or fit data to the surface of a sphere so they are used widely in Earth sciences to represent potential fields like gravity or the magnetic field.

From the available standardized models here the World Magnetic Model for 2015-2020 (WMM2015) was used. This model is maintained by the National Geophysical Data Center and the British Geological Survey and updated in 5-year intervals [11]. It models the field produced by Earth's core (called the main field), secular variations but does not deal with the effects of the crust and mantle and fields originating outwards from the surface, called disturbance fields. We can write the magnetic field \mathbf{B} as the negative gradient of the scalar potential V , both functions of latitude, longitude, altitude and time:

$$\mathbf{B}(\phi, \lambda, h, t) = -\nabla V(\phi, \lambda, h, t) \quad (2.28)$$

The potential is then expanded into spherical harmonic terms:

$$V(\phi, \lambda, h, t) = a_g \sum_{n=1}^N \left(\frac{a_g}{r} \right)^{n+1} \sum_{m=0}^n (g_n^m(t) \cos(m\lambda) + h_n^m(t) \sin(m\lambda)) P_n^m(\sin \phi) \quad (2.29)$$

Here, $a_g = 6371200$ m is the geomagnetic reference radius, $N = 12$ is the order of the model, g_n^m and h_n^m are time-dependent Gauss coefficients, which are obtained from measurements and P_n^m is a special

function called a Schmidt semi-normalized associated Legendre function.

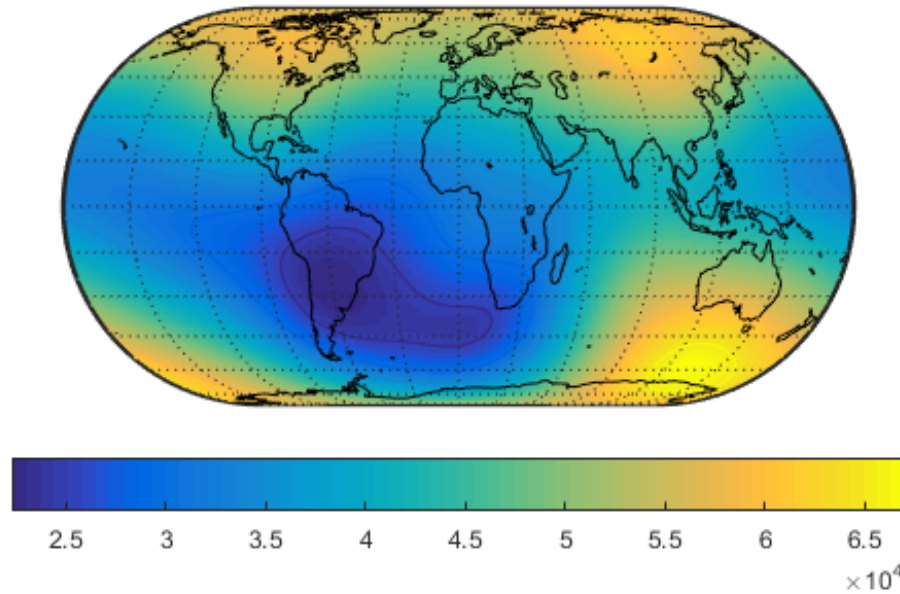


Figure 2.8: WMM2015 main field intensity at the altitude of 650 km [nT]

The WMM produces a magnetic field shown on Fig. 2.8. The model is valid from -1 km to 850 km altitude above the WGS84 ellipsoid. The global estimated model uncertainty is 134 nT in total field strength, which includes the uncertainties from the crustal field, secular variation and more importantly, the disturbance fields. In this work the MATLAB implementation of WMM, the `wrldmagm` function is used.

2.5.2 Gravity gradient torque

A small torque can be derived from Newton's law of gravitation if we treat the satellite as a body with volume rather than a point mass. Different parts of the satellite will experience different gravitational forces depending on the small distance differences from other bodies. Since gravitational force diminishes with the square of the distance other sources than the primary body (Earth for LEO satellites) can be

disregarded. The resulting torque around the center of mass is:

$$\mathbf{T}_g = \int_B \mathbf{R} \times d\mathbf{F}_g \quad (2.30)$$

where R is the position vector of the mass element and $d\mathbf{F}_g$ is the gravitational force on the mass element dm calculated as:

$$d\mathbf{F}_g = -\frac{Gm_{Earth}}{|\mathbf{R}|^3} \mathbf{R} dm \quad (2.31)$$

Equation 2.30 can be rewritten by writing the position vector using the center of mass position as $\mathbf{R} = \mathbf{R}_C + \mathbf{r}$ which can be further manipulated to yield the following well-known equation [12]:

$$\mathbf{T}_g = \frac{3Gm_{Earth}}{|\mathbf{R}_C|^5} \mathbf{R}_C \times [I] \mathbf{R}_C \quad (2.32)$$

In Eq. 2.32 all vectors are taken in the body frame so that the term $[I]$, which is the inertia matrix of the satellite will also be in the body frame where it is constant (assuming the satellite is treated as a rigid body).

2.5.3 Atmospheric drag torque

Satellites in Low-Earth Orbit still experience significant drag from the atmosphere. For larger satellites, this is a concern mainly for the mission lifetime as air drag causes orbital decay but is significant for nanosatellites due to their usually limited control authority. The atmospheric drag force can be calculated using the well-known formula:

$$\mathbf{F}_{atm} = -\frac{1}{2} c_D \rho A_{proj} \mathbf{v}^2 \quad (2.33)$$

where c_D is the satellite drag coefficient, A_{proj} is the projected area and v is the velocity vector. The velocity vector in the OCF frame has the form $\mathbf{v}_{OCF} = [v \ 0 \ 0]$ so it is a convenient choice to calculate the drag force. Now we need to characterize the different terms. The torque can be calculated from the position of the center of pressure r_{CP} with respect to the center of mass:

$$\mathbf{T}_{atm} = \mathbf{r}_{CP} \times \mathbf{F}_{atm} \quad (2.34)$$

The Knudsen number Kn is used to classify the flow based on mean free path λ_f and physical length scale L :

$$Kn = \frac{\lambda_f}{L} \quad (2.35)$$

The transition from continuum mechanics to free molecular flow is usually placed at $Kn > 10$ [13] and In LEO conditions λ_f is in the order of 10^5 meters, while the physical length scale is in the order of 10^{-9} meters so it is valid to treat the airflow as a free molecular flow. Under these conditions the usual assumption is that the satellite drag coefficient is constant with the value 2.2 [14]. This has been proven to be a good rule-of-thumb and will be used in this work as well.

To model the density distribution in the upper atmosphere we will use an empirical density model called NRLMSISE-00. This is part of a class of models called Mass Spectrometer Incoherent Scatter Radar (MSIS) models [15]. Other models widely used are the Jacchia-1970 (J70) model and the 1976 US Standard Atmosphere (USSA). The J70 model is based on observation of orbital decay of objects. The USSA model is a lapse-rate model with similar methodology as the International Standard Atmosphere but validity up to 1000 km altitude. The model requires several space weather parameters besides LLA coordinates, namely the daily F10.7, the 3-month average F10.7 and the daily Ap index values. The Ap index represents the daily global geomagnetic activity level derived from multiple measurement points over the globe. The F10.7 index represents the noise level generated by the sun at the 10.7 cm wavelength at Earth's orbit. The global daily value of this index is measured at local noon at the Pentictin Radio Observatory in Canada. It is used as a measure of the solar output in wavelengths that produce photoionization in the upper atmosphere. Daily averages, forecast and time history of these values are available from NOAA [16]. Space weather influences the density significantly, as illustrated on Fig. 2.9 where density is plotted for low, average and high solar activity with historical data taken from [16].

The projected area is obtained using a raster-based method where the satellite geometry is rendered to an image which is then counted for pixels containing the satellite. Using the known reference area of the image, the projected area and the center of pressure coordinates can be calculated. This process is repeated for a large set of orientations which are then stored in a lookup-table which is used to interpolate values during runtime. A more detailed description is presented in Chapter 4.

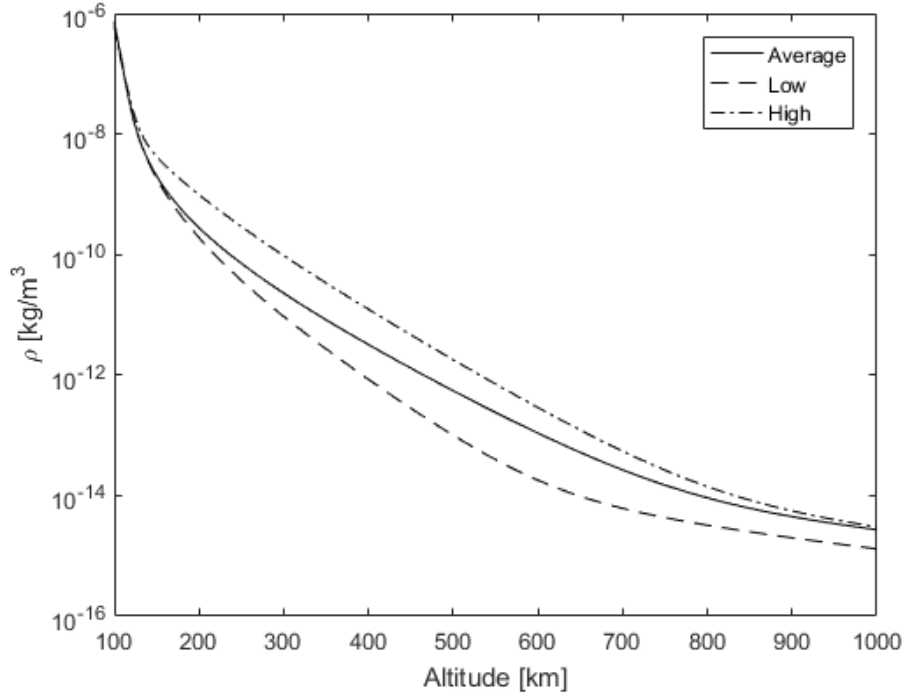


Figure 2.9: Atmospheric density output of the NRLMSISE-00 model as a function of altitude for historical mean, minimum and maximum solar activity.

2.5.4 Radiation pressure torque

Satellites also experience disturbance from the particle bombardment of the Sun. Technically all bodies emit radiation, but in practice the Sun is the only source which plays a measurable role in attitude dynamics so we will only consider that contribution. The Sun emits radiation as photons over a wide spectrum and energetic particles which make up the solar wind. A simple model for radiation pressure can be written similarly to the aerodynamic torque, first expressing the radiation pressure force:

$$\mathbf{F}_{rad} = -\nu \mathbf{p}_{rad} c_R A_{proj} \quad (2.36)$$

where A_{proj} is the projected area of the satellite, $c_R \simeq 1.2$ is the radiation pressure coefficient analogous to the drag coefficient, ν is the Earth shadow function, which has a value between 0 and 1 depending whether the satellite is illuminated or not. Finally, \mathbf{p}_{rad} is the radiation

pressure vector which is calculated as:

$$\mathbf{p}_{rad} = \frac{P_{sol}}{c} \hat{\mathbf{r}}_{\odot} \quad (2.37)$$

where P_{sol} is the solar constant, with a value of 1371 kW/m^2 on LEO, c is the speed of light in vacuum and \mathbf{r}_{\odot} is the position vector of the Sun in the given frame. Earth also reflects light to the satellite, this is referred to as albedo. Due to the geographically variable nature of albedo and the low contribution of radiation pressure to the overall disturbance torque, this effect is disregarded for the purposes of radiation torque modelling. The torque is calculated the same way as for the atmospheric drag torque:

$$\mathbf{T}_{rad} = \mathbf{r}_{CP} \times \mathbf{F}_{rad} \quad (2.38)$$

The Earth shadow function ν takes values between 0 and 1 for complete occlusion and full sunlight respectively. The model used here treats the Sun and Earth as two spheres, not accounting for oblateness and the atmosphere. The shadowing is proportional to the area blocked out by Earth from the Sun's disc. This results in a conical shadow geometry depicted on Fig. 2.10. The region where Earth completely blocks the Sun is called umbra where the function returns 0. The partially-shaded region is called the penumbra where the function returns a value based on the percentage visible from the Sun's disc. Using Earth-centered coordinates in the notation of Figure 2.10-2.11 we get $\mathbf{s} = \mathbf{r}_{ECI}$ and the shadow function can be written as [17]:

$$a = \arcsin \frac{R_{Sun}}{|\mathbf{r}_{Sun} - \mathbf{r}_{ECI}|} \quad (2.39)$$

$$b = \arcsin \frac{R_{Earth}}{|\mathbf{r}_{ECI}|} \quad (2.40)$$

$$c = \arccos \frac{-\mathbf{r}_{ECI} \cdot (\mathbf{r}_{Sun} - \mathbf{r}_{ECI})}{|\mathbf{r}_{ECI}| |\mathbf{r}_{Sun} - \mathbf{r}_{ECI}|} \quad (2.41)$$

$$\nu = \begin{cases} 0 & |a - b| \geq c \\ 1 - \frac{A}{\pi a^2} & |a - b| < c < a + b \\ 1 & c \geq a + b \end{cases} \quad (2.42)$$

In Eq. 2.42 the shaded area is calculated following the geometric notation from Fig. 2.11:

$$A = a^2 \arccos(x/a) + b^2 \arccos((c - x/b) - cy) \quad (2.43)$$

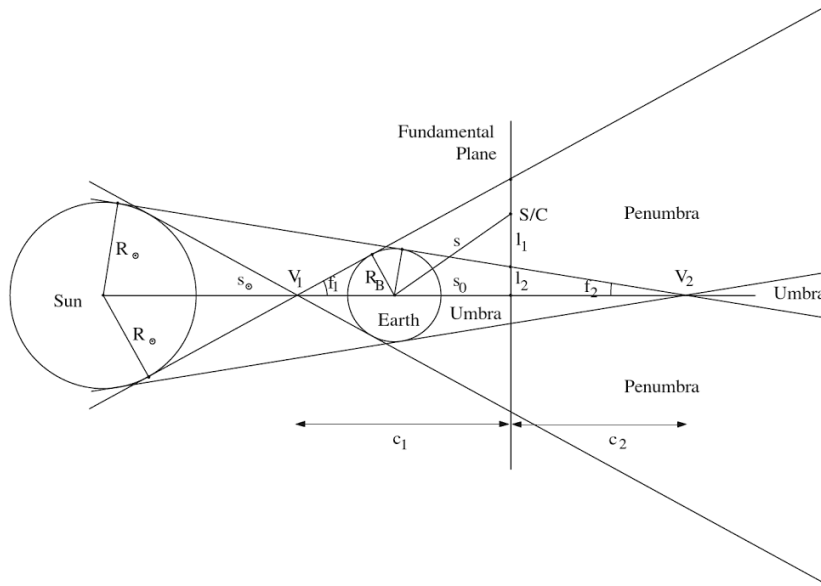


Figure 2.10: Conical Earth shadow geometry [17].

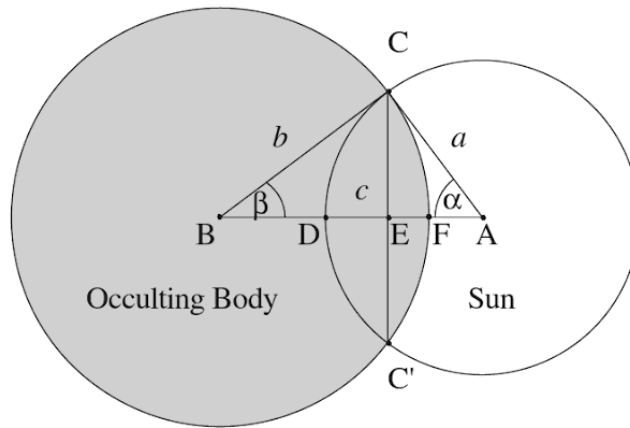


Figure 2.11: Conical Earth shadow geometry [17].

where

$$x = \frac{c^2 + a^2 - b^2}{2c} \quad \text{and} \quad y = \sqrt{a^2 - x^2} \quad (2.44)$$

The shadow model described here is used in the time-varying magnetic dipole moment calculations in Chapter 3.

Chapter 3

Magnetic Dipole Modelling

The main objective of this thesis is to provide an algorithm for the magnetic dipole compensation currents in order to achieve requirement 2.SYS.FR.17 in Table 1.1. Most CubeSat dynamical models assume that the dipole moment is constant [18] [19] and all further magnetic disturbances are handled by the controller as noise or unmodelled torque, which is a good approximation [20] [21] but due to the requirements in case of SEAM the ADCS torquers will not be powered during measurements thus a more detailed dipole model is used.

In this chapter, first the dipole sources are outlined, followed by a detailed description of the power system required in later steps. Finally, the proposed algorithm for on-board time-dependent control of the compensation current is described.

3.1 Magnetic Dipole Sources

The dipole moment on-board the satellite is built up from different sources. The two main components are the constant dipole from the satellite body and time-varying dipole from on-board current loops [22]. The generally applied solution is online estimation of dipole moment components using Kalman filtering alone or in combination with more advanced methods [23–25]. In [26,27] an EKF is used for estimation and in [28] an UKF estimator is described. In [29] an offline EKF method was described to estimate the constant part of the dipole moment and an online EKF estimator to handle the time-varying component. Recently in [30] an in-orbit but offline genetic algorithm method was described. In the present work we approach dipole moment mod-

elling from the analytical side and use developed disturbance models to estimate the dipole moment components offline on the ground.

The satellite will be degaussed before launch but a small constant dipole will remain. This is the previously mentioned residual magnetic dipole (RMD) moment of the satellite. The author is not aware of any published work done to characterise how the RMD moment changes over the lifetime of the satellite but is reasonable to assume that over long periods of time it will change (probably increase) due to residual magnetisation by Earth's magnetic field. Another smaller source can be dipole moment from magnetic hysteresis but this will be disregarded in the present work due to the slow system dynamics, complexities in modelling and low influence on the overall dipole.

The time-varying dipole moment produced by the current loops on-board the satellite can be obtained from the integral representation of the magnetic dipole moment itself:

$$\boldsymbol{\mu} \equiv I A \hat{\mathbf{n}}_A \quad (3.1)$$

where I is the current running in the loop, A is the loop area and $\hat{\mathbf{n}}_A$ is the surface normal defined by right-hand rule from the current. Combining the two sources and writing I as a function of time the total dipole of the satellite can be written as:

$$\boldsymbol{\mu}(t) = \boldsymbol{\mu}_c + \sum_{i=1}^N I(t)_i A_i \hat{\mathbf{n}}_{cell,i} \quad (3.2)$$

The next step is to analyse the power system and determine the possible current loops. The loop areas and normal vectors will be assumed to be constant in the Body frame since the geometry of the satellite is assumed to be rigid.

3.2 Power system

The power system of the satellite consists of solar cells, a Power Processing Unit (PPU) and a battery. The latter two are located in the last stack, close to the solar panel wings. Several steps were taken to reduce both the RMD and current-produced moments; all power supply cables are twisted pairs, material selection for connectors, cables and PCBs were based on EMC guidelines, and specifically the material of the battery and its casing was selected to be non-magnetic.

The magnitude of the RMD moment of the satellite (unpowered) was measured before and after degaussing and was found to be 48 mAm^2 before and 3.6 mAm^2 afterwards. During measurements only critical systems are powered to minimize interference thus we concentrate on the modelling of the largest-current active components which are the solar cells.

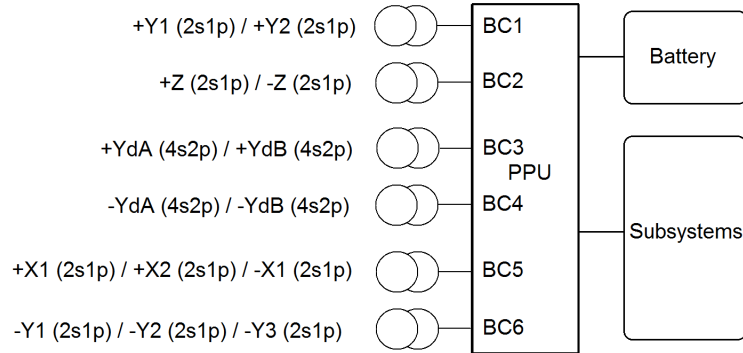


Figure 3.1: SEAM power system layout. Note that panel naming follows the CAD frame.

SEAM features a total of 52 solar cells for power generation feeding into 6 power ports (boost converters) on the PPU. The solar cells are triple junction type, connected in series of 2 or 4 with a blocking diode for each panel. Panels are connected in parallel and routed to one of the boost converters. The connections are shown on Figure 3.1 in the CAD coordinate frame, indicating the direction normal for each panel. The bracketed expression behind panel names tells the number of series and parallel connections on the panel and the / symbol denotes parallel connection between the panels. The dA and dB panels refer to ram and anti-ram directions on the wings, respectively. The wiring of the solar panels will cause some complications with the determination of the produced dipole moment when there are stray light sources which will be discussed in Chapter 4.

3.3 Solar cell model

To obtain the current flowing through a solar cell it is necessary to model the cell circuit. Figure 3.2 shows the electrical model of one cell. The cells on SEAM do not have bypass diodes, only a blocking diode

at the end of each series connection. The current through the cell can be written as [31]:

$$I(V, I_{pv}) = \frac{R_p(I_{d,sat} + I_{pv})}{R_s + R_p} - \frac{V}{R_s + R_p} - \frac{V_{d,t}}{R_s} W(\xi) \quad (3.3)$$

$$\xi = \frac{R_s R_p I_{d,sat}}{V_{d,t}(R_s + R_p)} \exp\left(R_p \frac{R_s I_{pv} + R_s I_{d,sat} + V}{V_{d,t}(R_s + R_p)}\right) \quad (3.4)$$

where R_s and R_p are the series and parallel resistance respectively, $V_{d,t}$ is the cut voltage and $I_{d,sat}$ is the saturation current of the diode. The function $W(z)$ is the Lambert W function. At the inputs V is the voltage of the cell, I_{pv} is the photovoltaic current which is a function of the illumination i , which itself is the function of the illumination angle α and the illuminated area ratio k of the cell:

$$I_{pv}(i) = i I_{pv}^{max} = \cos(\alpha) \frac{A_{ill}}{A_{cell}} I_{pv}^{max} = \cos(\alpha) k I_{pv}^{max} \quad (3.5)$$

At a given time, using the illumination values Eq. 3.5 can be used to generate the I-V curve of every solar cell on the satellite. The individual I-V curves are then added to produce the I-V curve of a whole boost converter circuit. The voltage of the BC circuit will be set by a Maximum Power Point Tracker (MPPT) on the PPU and will be assumed to find the ideal voltage with the maximum power. The BC voltage and current is then used to solve for the individual cell currents. Since the voltage is set by the system Eq. 3.5 shows that the individual cell currents and thus the magnetic dipole moment produced is only a function of the illumination of each cell.

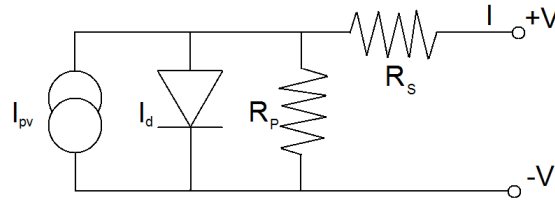


Figure 3.2: Solar cell circuit model.

3.4 Magnetic dipole compensation

The solar cell model described in Section 3.3 is a high resolution model of the time-varying dipole but as shown it requires the knowledge of

the illumination of each cell. Cell currents are not measured separately and there are only 12 sun sensors on the satellite to measure illumination so it is not possible to trivially acquire the individual light levels or currents of each cell. The satellite has two booms and solar cell wings which will cause significant self-shadowing. This is problematic because the sun sensors from a given side will not necessarily convey information about the illumination levels of all the cells on that side if the surface is partly shaded. The exception of this is the ram-direction solar panel because no other parts of the satellite can cast a shadow on it. The sun sensors are however, provide enough redundant information to reconstruct the Sun vector.

3.4.1 Compensation Algorithm

A simple model is presented to estimate the current-induced dipole from the solar panels and show that for only Sun illumination and known loop areas, it will produce the exact same torque as the detailed model. The motivation for this approach is that this model is lightweight to compute, requires few parameters which can be adjusted easily by telecommand system and it relies on very few assumptions about the environment of the satellite. First, consider the case where there is no stray light present from any other source (Earth, Moon albedo, reflected from other spacecraft surfaces). In this case let the produced dipole moment be:

$$\boldsymbol{\mu}_{panels} = \sum_{j=1}^6 I_{BC,j} \hat{\mathbf{n}}_{S,j} A_{c,j} n_{series} \quad (3.6)$$

where, $I_{BC,i}$ is the current measured at the $j : th$ boost converter, $A_{c,j}$ is the loop area per cell (assumed constant for a given BC loop), n_{series} is the number of cells in series on all panels and $n_{S,i}$ is defined as:

$$\hat{\mathbf{n}}_{S,i} = \text{sign}(\hat{\mathbf{n}}_i \cdot \hat{\mathbf{n}}_{Sun}) \hat{\mathbf{n}}_i \quad (3.7)$$

As seen from Equation 3.7 $n_{S,i}$ returns the Sun-facing surface normal. This is always the case due to the geometry of the satellite, on a given BC circuit the panels are all parallel to each other and their normals differ only by a sign. Thus we only need to find which panel of the two is illuminated by the Sun (the Sun vector is defined to point at the Sun in the Body frame). Still continuing along the assumption that there

are no other light sources, all the current will be produced on the Sun-facing panels of a given BC circuit. Since all the cells are identical the high-resolution model and this simplified model both give the same result:

$$\boldsymbol{\mu} = \sum_{panels} I_{cell,i} A_{c,i} \hat{\mathbf{n}}_{cell,i} = I_{BC,j} \hat{\mathbf{n}}_{S,j} A_{c,j} n_{series} \quad (3.8)$$

This is because the total current $I_{BC,j}$ is the sum of the parallel currents in $I_{cell,i}$ and the produced dipole is the same regardless if one of the panels in parallel is shadowed and all the current is produced by the other panel since the dipole is a linear function of the current. This equality was verified in the calculations, shown later in Chapter 4. Adding the RMD moment to Equation 3.9 yields the total dipole vector to be compensated. With a sign correction, the moment to be generated can be written as:

$$\boldsymbol{\mu}_{magbias} = -\boldsymbol{\mu}_{RMD,est} - \sum_{i=1}^6 I_{BC,i} \hat{\mathbf{n}}_{S,i} A_{c,i} n_{series} \quad (3.9)$$

3.4.2 Model limitations

The model will produce errors when there are other light sources present, which in real conditions is due mainly to Earth albedo. At the planned altitude of SEAM in LEO, Earth takes up a significant portion of the field of view (approx. 130 deg at 650 km) and cannot be treated as a point source (i.e. it can illuminate panels facing opposing directions). Without the knowledge of individual cell currents or a detailed Earth albedo model (which would be demanding on the OBC and would have to be updated daily) it is not feasible to compensate this effect. The magnitude of albedo-produced moment is significantly smaller than the moment from solar illumination. Additionally, since the satellite is assumed to be within 10 degrees to the LVHV frame stray light is expected to hit opposing sides of the satellite due to the large field of view which will help diminish this effect. In Chapter 4 the disturbing effects of Earth albedo are investigated in more detail.

Chapter 4

Implementation

This chapter details the attitude simulation tool developed for this thesis, followed by the implementation and evaluation of the compensation algorithm defined in Section 3.4. The simulation package was built in MATLAB and has two main pipelines for satellite attitude modelling; one for forward attitude simulation and one for parameter reconstruction from telemetry. Special care was given to easily represent complex geometries to capture the self-shadowing effects as they are important to describe the time-varying dipole. The design principle was maximum flexibility with high performance. In the finished software it is very easy to swap disturbance models, environments or satellite models while maintaining low integration times.

4.1 Simulation setup

To run either of the models, three things have to be defined: the satellite, the environment and the initial attitude. These are all represented as instances of a distinct object class. The three base objects are contained in a simulation object along with additional parameters. The object model diagram used by the software can be seen on Fig. 4.2. After the simulation object is constructed, the integrator can be called, which is the `ode45` solver. As seen from the object diagram the model uses the state vector:

$$x = [\mathbf{q}, \boldsymbol{\omega}] = [q_0, q_1, q_2, q_3, q_4, \omega_1, \omega_2, \omega_3] \quad (4.1)$$

which leads to the following initial value problem:

$$\frac{dx}{dt} = f(t, x, P), \quad x(t_0) = x_0, \quad t \in [t_0, t_{sim}] \quad (4.2)$$

where P are extra parameters passed to the solver as an instance of the `attitudeSimulationClass` object and t_{sim} is the simulation time. The nonlinear ODE system in $f(t, x, P)$ is the combination of Eq. 2.25-2.26.

4.1.1 Satellite

The satellite object contains the physical properties of the spacecraft. Table 4.1. For the aerodynamics and radiation model as well as the solar cell current simulation we need information on the visible surfaces and areas of the satellite and its components. This data is stored in attitude-indexed lookup tables for each component. The calculation is done via a raster-based algorithm which will not yield the exact areas but can handle arbitrary geometries. Since SEAM has a fairly complex concave geometry this approach was deemed favorable. To define the geometry and build the lookup tables a GUI tool was developed. It is possible to import `.stl` geometry directly to the software. When a new component is specified the geometry is stored in the component structure as seen on Fig. 4.2 along with information on the surface normal and type. On Fig. 4.1 is an example of the software. After specifying

Parameter	Value			
Satellite mass	3.720 <i>kg</i>			
Inertia matrix (in CAD frame)	$\begin{bmatrix} 0.094 & 0.001 & -0.001 \\ 0.001 & 0.645 & 0.000 \\ -0.001 & 0.000 & 0.592 \end{bmatrix}$			<i>kgm²</i>
Center of mass (in CAD frame)	$\begin{bmatrix} 26.4 & 0.4 & -49.6 \end{bmatrix}$			<i>mm</i>
Drag coefficient	2.2			
Radiation pressure coefficient	1.0			

Table 4.1: SEAM physical properties.

ing the geometry and setting the lookup table size through the angular

resolution controls, it is possible to simplify the geometry. This is advised if the full CAD model was imported for satisfactory calculation performance. Before beginning the calculation the coordinate system should be checked using the view controls. During calculation MAT-

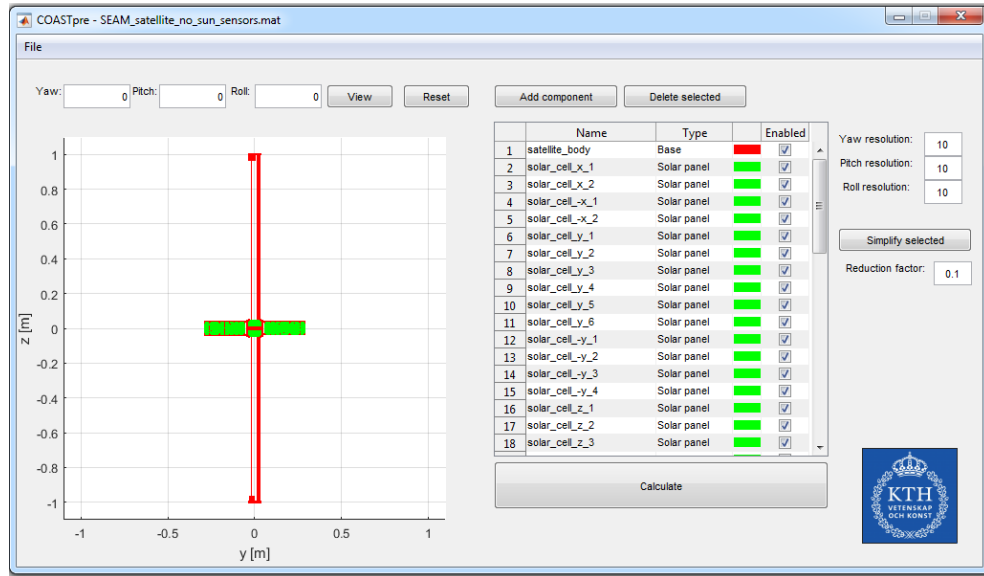


Figure 4.1: Geometry pre-processing software.

LAB creates a hidden figure windows to render the satellite in higher resolution. The size of this window is limited by the screen size and is set to 1000-by-1000 pixel by default. Larger resolutions are possible to work-around but the computational time will increase with the $\mathcal{O}(n^2)$ of the resolution n . The visible projected areas are calculated from counting component pixels from the rendered image and stored in the `AprojMatrix` field of the component. The projection center point coordinates are also calculated and stored in the `textttrCPMatrix` field. This includes conversion from MATLAB screenspace coordinates the projection frame.

4.1.2 Environment

The environment object requires to specify the TLE file used and a cell array of torque function handles. The input-output format of disturbance functions is uniform so they can be dynamically included or removed. The functions have access to all simulation parameters. Additionally to the environmental disturbance models detailed in Chap-

ter 2 there is an exponential atmosphere aerodynamic torque model and an IGRF-based magnetic disturbance model. The standard disturbance torque setup used will be the following:

- Gravity gradient: point mass model (Eq. 2.32)
- Magnetic dipole torque: constant RMD and time-varying solar cell current-produced moment with WMM magnetic field
- Aerodynamic torque: NRLMSISE-00 density
- Radiation pressure: constant sources from the Sun and Earth, conical Earth shadow geometry

4.1.3 Pointing

The attitude object constructor requires an input attitude, body angular rate and the previously-defined environment object. It supports ECI-to-Body or OCF-to-Body input frames and either 3-2-1 Euler angles or quaternions as input. Since the pointing requirement is specified with respect to the OCF frame usually the attitude is initialized with respect to this frame using 3-2-1 Euler angles. The transformation process starts by converting the Euler angles to quaternions by combining Eq. 2.13, 2.8-2.9 and 2.15 yielding

$$\mathbf{q} = \begin{bmatrix} \cos(\phi/\theta/2) \cos(\theta/2) \cos(\psi/2) + \sin(\phi/\theta/2) \sin(\theta/2) \sin(\psi/2) \\ \cos(\phi/\theta/2) \cos(\theta/2) \sin(\psi/2) - \sin(\phi/\theta/2) \sin(\theta/2) \cos(\psi/2) \\ \cos(\phi/\theta/2) \sin(\theta/2) \cos(\psi/2) + \sin(\phi/\theta/2) \cos(\theta/2) \sin(\psi/2) \\ \sin(\phi/\theta/2) \cos(\theta/2) \cos(\psi/2) - \cos(\phi/\theta/2) \sin(\theta/2) \sin(\psi/2) \end{bmatrix} \quad (4.3)$$

which can then be translated from OCF to the ECI frame. This requires the quaternions to be transformed to a DCM as:

$$[C] = \begin{bmatrix} q_0^2 + q_1^2 - q_2^2 - q_3^2 & 2(q_1q_2 + q_0q_3) & 2(q_1q_3 - q_0q_2) \\ 2(q_1q_2 - q_0q_3) & q_0^2 - q_1^2 + q_2^2 - q_3^2 & 2(q_2q_3 + q_0q_1) \\ 2(q_1q_3 + q_0q_2) & 2(q_2q_3 - q_0q_1) & q_0^2 - q_1^2 - q_2^2 + q_3^2 \end{bmatrix} \quad (4.4)$$

This can now be multiplied by the DCM transforming from ECI to OCF from Eq. 2.23 to yield the ECI-to-Body DCM as:

$$[C]_{ECI,Body} = [C]_{OCF,Body} [C]_{ECI,OCF} \quad (4.5)$$

The DCM $[C]_{ECI,OCF}$ requires the knowledge of the ECI position and velocity vector which are obtained by running the orbit propagation algorithm with zero propagation time. The last step is to convert the result back into quaternions. This is done using Markley's algorithm [32] which is a modification of the classic Shepperd algorithm [33] but guarantees that the resulting matrix will be orthogonal. There are two steps involved in the algorithm; first we calculate the vectors $\mathbf{x}_{1...4}$:

$$\begin{aligned} \mathbf{x}_1 &= \begin{bmatrix} 1 + C_{11} + C_{22} + C_{33} \\ C_{23} - C_{32} \\ C_{31} - C_{13} \\ C_{12} - C_{21} \end{bmatrix} & \mathbf{x}_2 &= \begin{bmatrix} C_{23} + C_{32} \\ 1 + C_{11} - C_{22} - C_{33} \\ C_{12} + C_{21} \\ C_{13} + C_{31} \end{bmatrix} \\ \mathbf{x}_3 &= \begin{bmatrix} C_{31} - C_{13} \\ C_{12} + C_{21} \\ 1 + C_{22} - C_{33} - C_{11} \\ C_{23} + C_{32} \end{bmatrix} & \mathbf{x}_4 &= \begin{bmatrix} C_{12} - C_{21} \\ C_{31} + C_{13} \\ C_{23} + C_{32} \\ 1 + C_{33} - C_{11} - C_{22} \end{bmatrix} \end{aligned} \quad (4.6)$$

Then we take $\mathbf{x} = \max(\mathbf{x}_1(1), \mathbf{x}_2(2), \mathbf{x}_3(3), \mathbf{x}_4(4))$ and the quaternion is obtained as

$$\mathbf{q} = \frac{\mathbf{x}}{|\mathbf{x}|} \quad (4.7)$$

The angular momentum does not need to be transformed as it will always be defined in the Body frame so this provides the complete initial state \mathbf{x}_0 .

4.2 Results

In this section the performance and evaluation of the whole code is presented, starting with the forward model. Afterwards we present the results from the RMD moment estimation which uses the attitude simulated in the forward model as measured input.

4.2.1 Forward model without compensation

The forward model can be used to simulate the satellite response to the torques. The state vector then can be fed to the parameter estimator. Alternatively, after estimation the forward model is used to check

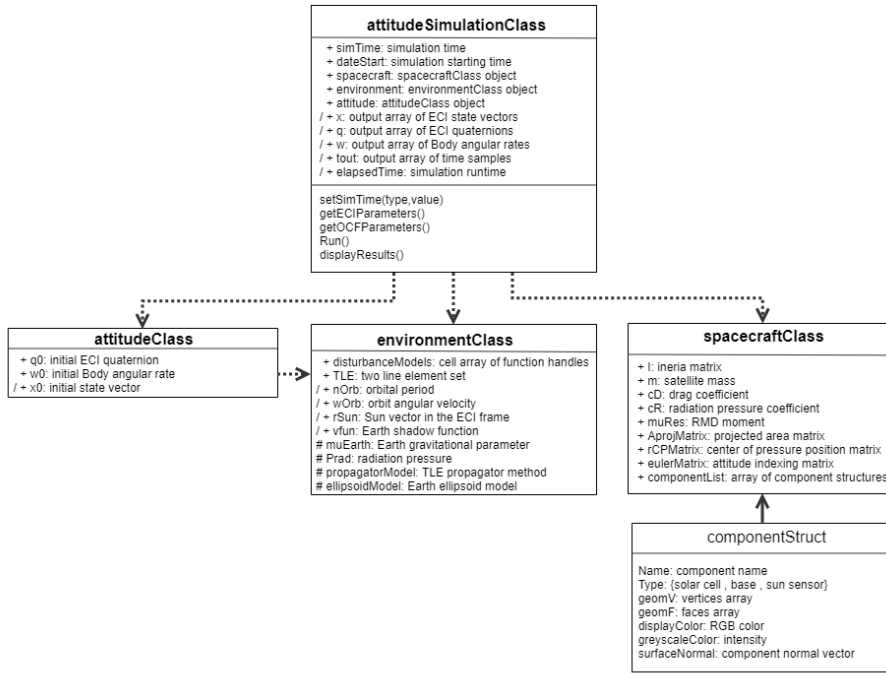


Figure 4.2: attitudeSimulationClass UML 2 object diagram.

the performance of the dipole compensator. A typical response for the nominal simulation case described in section can be seen on Figure 4.3 with the OCF-to-Body Euler angles and the Body angular rate vector components for a full orbit. The RMD moment was set to a low $[5 \ 5 \ 5] \text{ mAm}^2$.

Yawing motion seems to be dominant as expected due to the gravity gradient stabilization on the other axes provided by the booms. The yaw rate is unfortunately increasing and the system behaves unstably if left without active control for extended periods of time. The aerodynamic stability provided by the wings is not sufficient to keep the satellite from winding up. The angular rates on Figure 4.4 show this rate buildup on the z-axis along with the initial angular rate on the y-axis which is equal to the rate of the OCF frame. The magnetic torques on the spacecraft are shown on Figure 4.5. At the start of the simulation the satellite is in eclipse so there are no current-produced moments. At approximately $t = 1000 \text{ sec}$ the eclipse ends and the current produced dipole becomes the dominant disturbance.

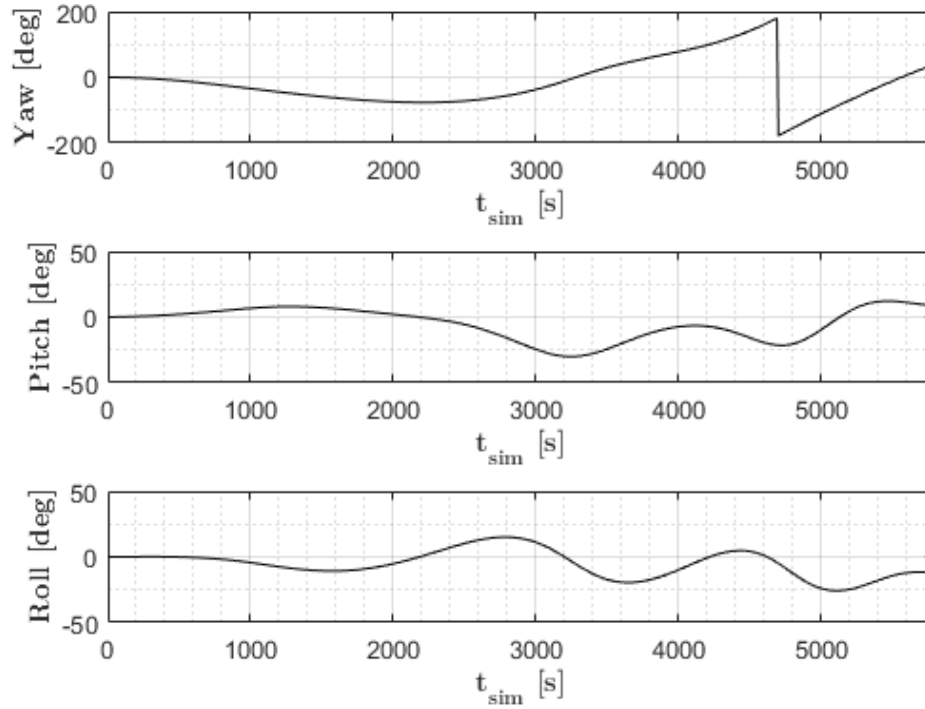


Figure 4.3: Simulated Euler angle attitude without dipole moment compensation.

4.2.2 RMD estimation

The results from the forward model are used to estimate the RMD moment components using a least-squares approach. During operation the satellite telemetry is downlinked regularly. Once on the ground, the estimated state vector is used to reconstruct the disturbance torque by solving Eq. 2.25 for \mathbf{T} . This requires the derivative of the angular velocity vector which is obtained via backwards difference:

$$\frac{d\boldsymbol{\omega}}{dt}_i \approx \frac{\boldsymbol{\omega}_i - \boldsymbol{\omega}_{i-1}}{t_i - t_{i-1}} \quad (4.8)$$

Higher-order finite difference methods yielded worse results when the telemetry timesteps did not cover local peaks of the environmental torques. Figure 4.6 shows the difference between the reconstructed and ‘real’ torque from the nominal simulation in the Body frame. The RMD torque is then obtained by subtracting the estimated other disturbance torques (current-produced, atmospheric, radiation, gravity gradient). The result can be seen on Figure 4.7. It shows that the backwards difference does not propagate a significant error down to the

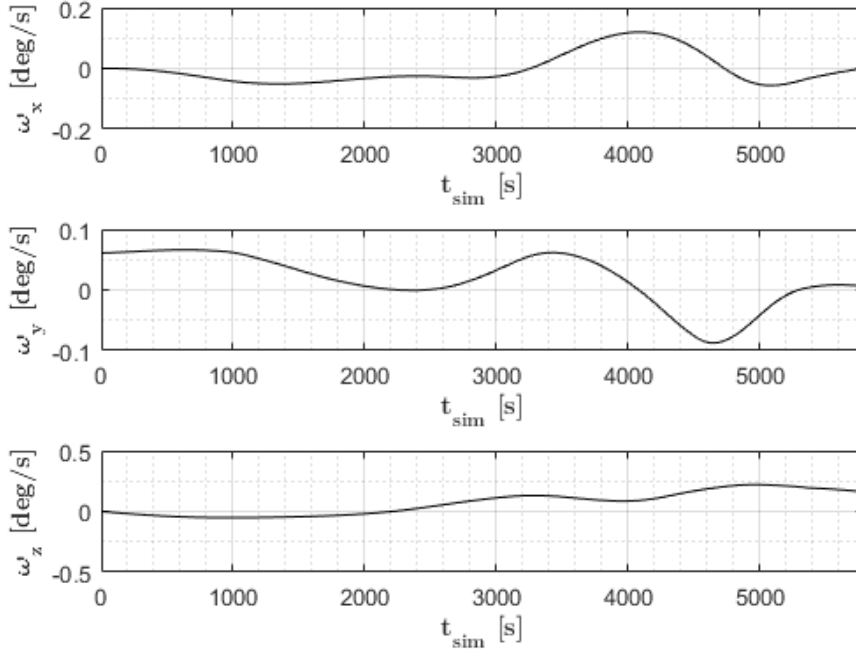


Figure 4.4: Simulated Body angular rates without dipole moment compensation.

torque estimation and does not seriously affect the reconstruction accuracy. The reconstructed RMD torque also has noise added from the estimated current-produced torque. This is most prominent where the current-produced torque has large changes, e.g. going in and out of eclipse.

The components of the RMD moment are then found by a linear regression. It requires the measured magnetic field \mathbf{B}_{Body} values along the estimated RMD torque vector. Using the relationship between the magnetic torque and dipole moment the equation system to be solved can be written in the form $y = Ax$ as:

$$\begin{aligned}
 \sum \begin{bmatrix} 2B_{z,i}^2 + 2B_{y,i}^2 & -2B_{x,i}B_{y,i} & -2B_{x,i}B_{z,i} \\ -2B_{y,i}B_{x,i} & 2B_{z,i}^2 + 2B_{x,i}^2 & -2B_{z,i}B_{y,i} \\ -2B_{x,i}B_{z,i} & -2B_{y,i}B_{z,i} & 2B_{x,i}^2 + 2B_{y,i}^2 \end{bmatrix} \begin{bmatrix} \mu_{x,est} \\ \mu_{y,est} \\ \mu_{z,est} \end{bmatrix} = \\
 = \sum \begin{bmatrix} 2T_{y,i}B_{z,i} - 2T_{z,i}B_{y,i} \\ -2T_{x,i}B_{z,i} + 2T_{z,i}B_{x,i} \\ 2T_{x,i}B_{y,i} - 2T_{y,i}B_{x,i} \end{bmatrix} \quad (4.9)
 \end{aligned}$$

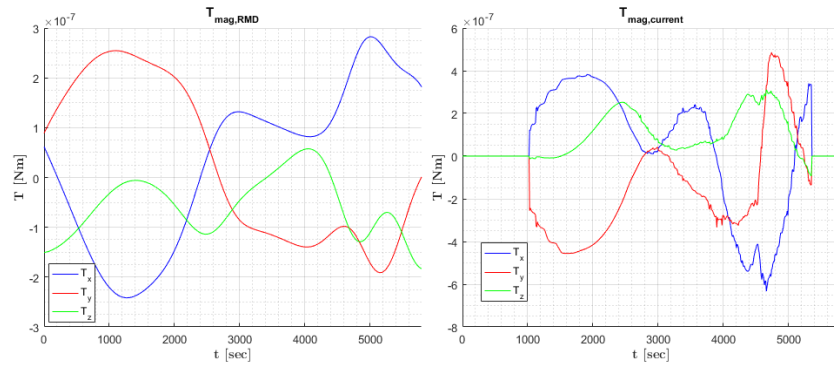


Figure 4.5: Simulated Body magnetic torques with the RMD torque (left) and the current-produced torque (right).

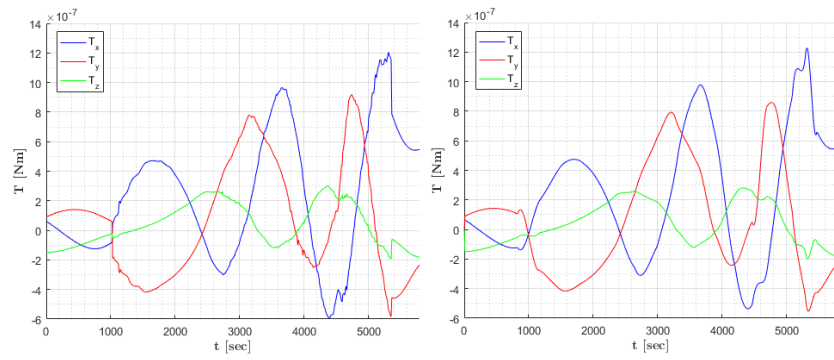


Figure 4.6: Body torque from forward model (left) and reconstructed torque from state vector (right).

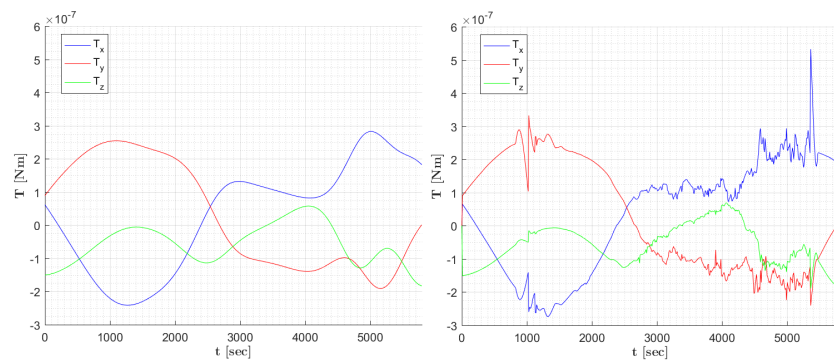


Figure 4.7: RMD torque from forward model (left) and reconstructed torque from state vector and estimated disturbances (right).

For the nominal case showed before this yields the RMD moment vector as:

$$\boldsymbol{\mu}_{RMD,est} = [5.06, 5.09, 4.47] \quad (4.10)$$

This corresponds to a total accuracy of 89.18 %. The error on the x and y axes is below 2 % and 10.6 % on the z axis. Now we will use this estimated dipole moment to run the forward model with dipole compensation.

4.2.3 Forward model with compensation

The dipole compensation algorithm is added as another torque source and the estimated RMD is set to $[5.06, 5.09, 4.47] \text{ mAm}^2$ but otherwise the simulation is identical to the one in Section 4.2.1. The Euler angle output is given on Figure 4.8. The yawing motion is still dominant but

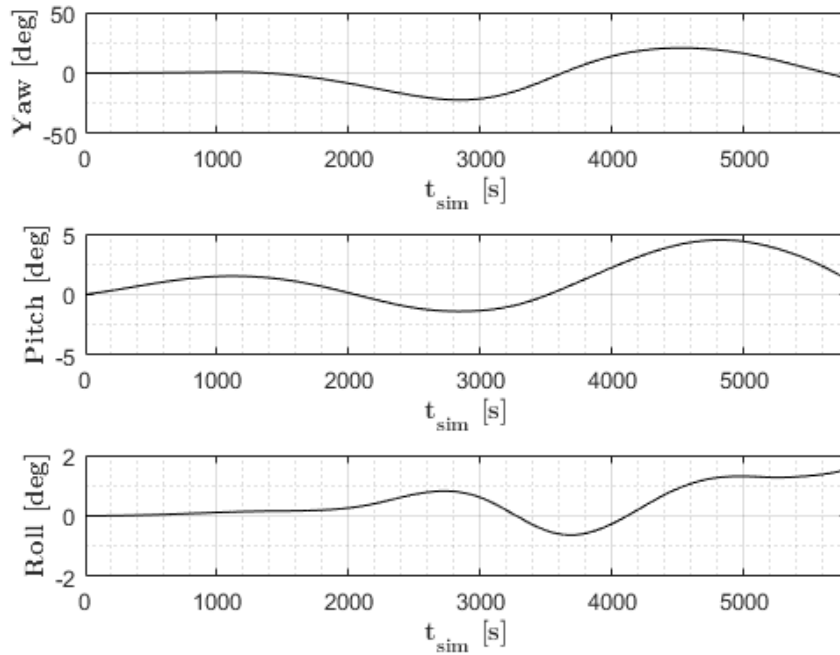


Figure 4.8: Simulated Euler angle attitude with dipole moment compensation.

the magnetic disturbance is reduced enough that the satellite does not start winding up. Comparing the time it takes to reach 10 *deg* angle error the compensated model gives 2078 sec versus the uncompensated

model at 491 sec. This leaves room for modelling errors and for the approximation errors of the compensation algorithm discussed in Section 3.4.2.

4.2.4 RMD estimation with albedo disturbances and sensor noise

To better approximate the real conditions the process outlined in the previous sections was modified to include modelling errors in the form of stray light from Earth albedo and instrument errors in the form of noise on the state vector fed into the attitude reconstruction process.

Stray light reflected from Earth generates additional current and thus dipole. In a simple model of the effect Earth is modeled as a spherical light source with the radiation constant $P_{rad,E} = 0.3P_{rad} = 411.3 \text{ kW/m}^2$ which is an average value for albedo. Due to the large apparent size of the planet and to decrease calculation time, self shading is disregarded. The added illumination for a given cell will be calculated as:

$$\Delta i_{cell} = \begin{cases} 0.3 \cos(\alpha - \delta/2) & \text{if } \alpha_{cell} > \delta/2 + \pi/2 \\ 0 & \text{otherwise} \end{cases} \quad (4.11)$$

where α_{cell} is the angle between the panel normal and Earth's position vector in the Body frame as

$$\alpha_{cell} = \arccos(\hat{\mathbf{n}}_{cell} \cdot \hat{\mathbf{n}}_{Earth}) \quad (4.12)$$

and $\delta/2$ is the half-cone angle of Earth's disc, calculated from the angular distance with Earth's diameter R_E and the satellite altitude h as:

$$\delta = 2 \arcsin\left(\frac{R_E}{R_E + h}\right) \quad (4.13)$$

Instrument noise is also added to the output as Gaussian noise on the Euler angles with zero mean and a standard deviation of the required attitude knowledge accuracy of 1 arcminute. The noise on angular velocity components is also zero mean and 0.02 degree/s standard deviation in all components.

It was mentioned at the limitations of the presented compensation algorithm that the effect of Earth albedo cannot be easily modeled but

the algorithm should be robust enough to still give satisfactory results. To verify this, the simple stray light is added to the forward model in the first step to generate the state vector and add the noise models to it before feeding it into the attitude reconstruction process. All simulation parameters except the dipole moment vector are the same as the nominal case. The reconstruction process does not include any model for the albedo. The result is then compared to the real dipole moment to characterize the estimation accuracy. This was repeated to a large number of sample dipole moment vectors to obtain an estimation sensitivity depending on the magnitude of the RMD moment. Figure 4.9 shows the absolute dipole estimation error in mAm^2 as a function of the dipole moment components.

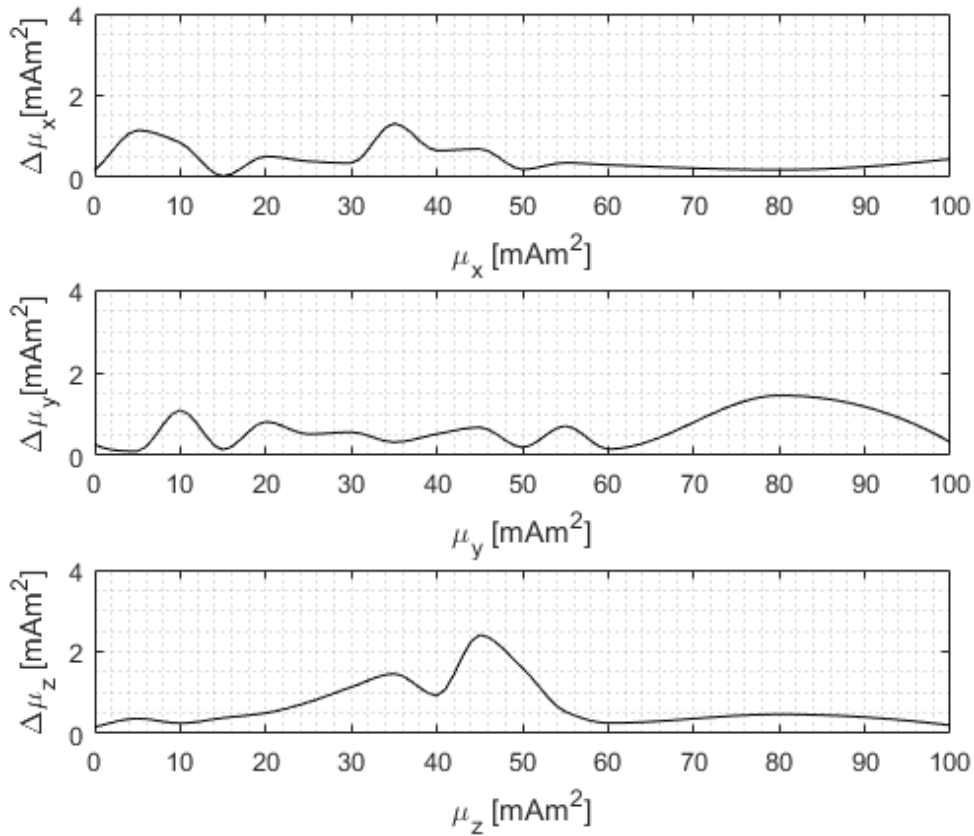


Figure 4.9: RMD estimation error as a function of component magnitude.

The largest estimation error is on the z axis in the 35-50 mAm^2 component magnitude range. The estimation error remains under 1 mAm^2

when the dipole is in the 0-20 mAm^2 range. The satellite is expected to have an RMD moment below 48 mAm^2 which lies in the maximum range of the z component. The maximum estimation error from the calculations is 5.18 mAm^2 if the worst performance is taken on all axes.

If the worst-case uncanceled dipole is assumed with the above magnitude the forward model gives an estimated 941 seconds coasting time which would be a bit less than the required 1000 seconds. However, this is not expected to occur as the corresponding RMD vector has elements well outside the expected RMD values. Inside the expected range it was found that the reconstruction performance gives the worse results if the dipole vector has a small angle with the z axis. The mean of the total estimation error is 1.81 mAm^2 . If the mean value of is assumed for estimation errors the forward model gives 1370 seconds of coasting time.

To conclude, the results show that the worst possible case is coming close to the required coasting time and the mean results meet the requirement with a 30% margin.

4.3 Simulation errors

The model of the satellite dynamics built and used in this work is not a perfect reproduction of reality. Most of the disturbance calculations are based on empirical models and some disturbances were omitted from the model. The `ode45` solver gives a numerical approximate to the solution of the ODE system and will add to the final calculation error. There is also uncertainty involved with all of the physical parameters and initial conditions. The projected area calculation introduces an error through the rasterization process. To quantify this the calculation was done on several simple test shapes with known dimensions. This error is found to be inversely proportional to the characteristic length of the geometry feature which is shown on Fig. 4.10. The smallest features on the model are the antennas on the first stack, these have a diameter of 3 mm which corresponds to 1.63 % error in the calculated area. The solar cells shorter sides are 40 mm with 1.02 % error. This error source can be further lowered to an arbitrary level at the cost of computational time by increasing the rasterization resolution. The numerical error of the ODE solver can be set with the absolute and relative tolerance of the solver. The relative tolerance specifies the

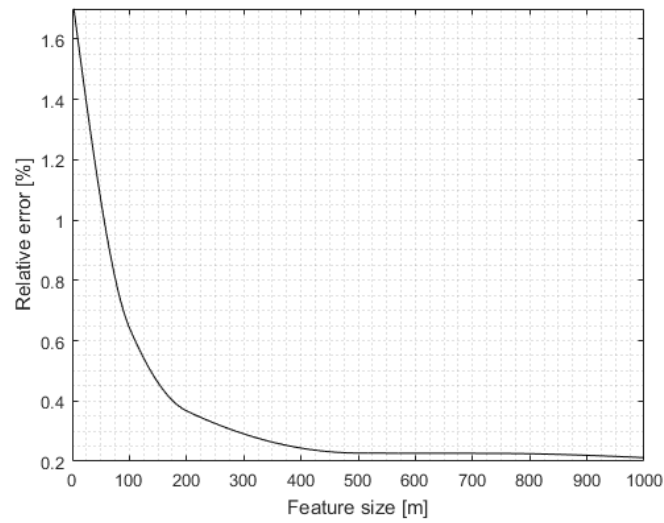


Figure 4.10: Relative area error as a function of feature size.

relative error for each of the solution vector components. Absolute tolerance is a cutoff threshold below which the value of a solution vector component does not matter.

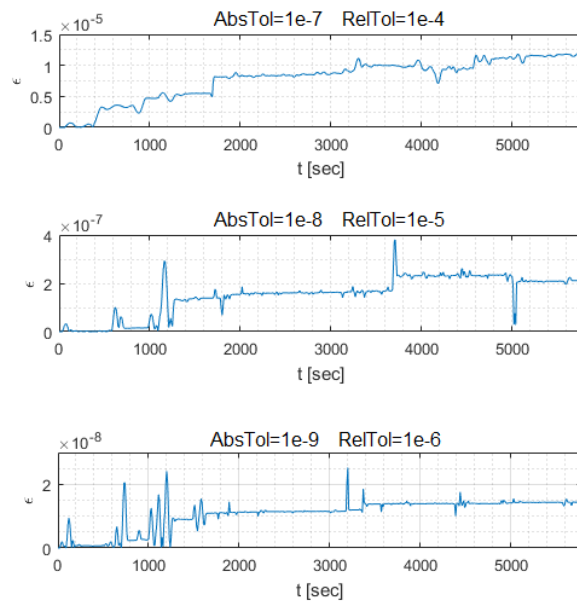


Figure 4.11: Quaternion error growth for the nominal simulation with different absolute and relative tolerance ODE solver settings.

The resulting error can be calculated as the difference between the output quaternion length and 1 since the attitude quaternion is a unit vector. Figure 4.11 shows the quaternion errors as a function of simulation time for different relative and absolute tolerance settings.

The error growth has jumps in it where the satellite is entering and exiting from eclipse. Since the simulation is not required to run for prolonged times the values chosen were 10^{-7} for absolute and 10^4 relative tolerances.

Chapter 5

Conclusion

In this master thesis a detailed attitude dynamics simulation of the SEAM satellite was performed for the uncontrolled coasting phase with a time-varying model for describing the magnetic dipole moment. A method to estimate the magnetic moment vector from the state vector was described. This was used as an input for a simple and robust dipole compensation algorithm to achieve the required coasting time while staying within the pointing requirements. The main conclusion is that the dipole moment vector can be estimated and compensated with sufficient accuracy to enable the satellite to achieve mission requirements. The developed software package is also usable for general ADCS analysis of other spacecraft.

The two main components of the dipole moment vector were compensated separately. The constant RMD moment has to be estimated from the telemetry offline, but once the components are available compensation is straightforward. The time-varying dipole strength is a function of the on-board currents and cannot be exactly measured due to the limitations from the electrical system layout. It is possible to cancel this out sufficiently with the proposed dipole compensation algorithm so that mission requirements are met, even in the presence of other environmental disturbances.

5.1 Estimation

The RMD components could be recovered with a mean accuracy of $1.81 \text{ mA}\cdot\text{m}^2$ which is enough for the compensation algorithm to keep the satellite within 10 degrees of the LVLH frame for 1300 seconds. The

presence of unmodelled disturbances and sensor noise decrease the performance of the estimation. It was noted that the estimation performance was better during eclipses as there were disturbances due to direct and reflected sunlight. During real-world conditions, telemetry gathered in eclipse is expected to give better results as well thus telemetry from these intervals is of high interest.

5.2 Compensation

The time-varying part of the compensation algorithm does not depend on any of the models used and only has the current loop areas as parameters which are not expected to change as that would imply that the structural integrity of the satellite is compromised. The constant part of the algorithm should be updated from estimation regularly as there is insufficient data available on how the RMD moment evolves over the lifetime of a satellite.

5.3 Further work

It is important to know the limitations of the model, therefore further investigation is required to quantify error sources and uncertainties. The satellite model can and should be refined once real telemetry is available. The algorithm presented here needs to be coded on the satellite OBC and the offline calculation tools should be streamlined to make it easy to process telemetry. For this, the ADCS telemetry format should be defined. Other sensor information, not used in estimation, i.e. sun sensor readings and temperature measurements could provide useful to increase the offline model accuracy. Finally, the inertia matrix and center of mass coordinates of the satellite should be measured more accurately before launch to reduce the associated parameter uncertainty.

Bibliography

- [1] Arash Mehrparvar, D Pignatelli, J Carnahan, R Munakat, W Lan, A Toorian, A Hutputanasin, and S Lee. Cubesat design specification rev 13. *The CubeSat Program, Cal Poly San Luis Obispo, US*, 2014. 1, 2
- [2] Kulu Erik. Nanosatellite database, 2017. 2
- [3] Åke Forslund, Serhiy Belyayev, Nickolay Ivchenko, Göran Olsson, Terry Edberg, and Andriy Marusenko. Miniaturized digital fluxgate magnetometer for small spacecraft applications. *Measurement Science and Technology*, 19(1):015202, 2007. 4
- [4] Hanspeter Schaub and John L Junkins. *Analytical mechanics of space systems*. AIAA, 2003. 9, 10, 11, 21
- [5] Jack B Kuipers et al. *Quaternions and rotation sequences*, volume 66. Princeton university press Princeton, 1999. 13
- [6] Felix R Hoots, Ronald L Roehrich, and TS Kelso. Spacetrack report no. 3. *Project Spacetrack Reports, Office of Astrodynamics, Aerospace Defense Center, ADC/DO6, Peterson AFB, CO, 80914*, 1980. 14, 15
- [7] David A Vallado, Paul Crawford, Richard Hujsak, and TS Kelso. Revisiting spacetrack report# 3. *AIAA*, 6753:2006, 2006. 14
- [8] Gérard Petit and Brian Luzum. Iers conventions (2010). Technical report, BUREAU INTERNATIONAL DES POIDS ET MESURES SEVRES (FRANCE), 2010. 16
- [9] John H Seago and David A Vallado. Coordinate frames of the u.s. space object catalog. *Astrodynamics Specialist Conference and Guidance, Navigation, and Control Conference*, 2000. 16

- [10] WM Mularie. Department of defense world geodetic system 1984, its definition and relationships with local geodetic systems. *National Geospatial-Intelligence Agency, Tech. Rep*, 152, 2000. 17
- [11] Arnaud Chulliat, Susan Macmillan, Patrick Alken, Ciaran Beggan, Manoj Nair, Brian Hamilton, Adam Woods, Victoria Ridley, Stefan Maus, and Alan Thomson. The us/uk world magnetic model for 2015-2020. 2015. 22
- [12] William E Wiesel. *Spaceflight [Space flight] dynamics*. McGraw-Hill, third edition edition, 2010. 24
- [13] Normand M Laurendeau. *Statistical thermodynamics: fundamentals and applications*. Cambridge University Press, 2005. 25
- [14] GE Cook. Satellite drag coefficients. *Planetary and Space Science*, 13(10):929–946, 1965. 25
- [15] JM Picone, AE Hedin, D Pj Drob, and AC Aikin. Nrlmsise-00 empirical model of the atmosphere: Statistical comparisons and scientific issues. *Journal of Geophysical Research: Space Physics*, 107(A12), 2002. 25
- [16] National Oceanic and Atmospheric Administration. Space weather prediction center, 1996. 25
- [17] Oliver Montenbruck and Eberhard Gill. *Satellite orbits: models, methods and applications*. Springer Science & Business Media, 2012. 27, 28
- [18] DC Maessen. Development of a generic inflatable de-orbit device for cubesats. 2007. 29
- [19] Jiewei Zhou. Attitude determination and control of the cubesat mist. 2016. 29
- [20] S Busch, P Bangert, S Dombrovski, and K Schilling. Uwe-3, in-orbit performance and lessons learned of a modular and flexible satellite bus for future pico-satellite formations. *Acta Astronautica*, 117:73–89, 2015. 29
- [21] James Armstrong, Craig Casey, Glenn Creamer, and Gilbert Dutchover. Pointing control for low altitude triple cubesat space darts. 2009. 29

- [22] Tomoya Suehiro. Satellite design methodology to suppress time-varying residual magnet effects on attitude for nano-satellites. *IFAC Proceedings Volumes*, 43(15):241–246, 2010. 29
- [23] Halil Ersin Soken, Shin-ichiro Sakai, and Rafal Wisniewski. In-orbit estimation of time-varying residual magnetic moment. *IEEE Transactions on Aerospace and Electronic Systems*, 50(4):3126–3136, 2014. 29
- [24] Halil Ersin Soken and Shin-ichiro Sakai. Multiple-model adaptive estimation of time-varying residual magnetic moment for small satellites. *Advances in Aerospace Guidance, Navigation and Control*, pages 303–321, 2015. 29
- [25] Shin-ichiro Sakai, Yosuke Fukushima, and Hirobumi Saito. Design and on-orbit evaluation of magnetic attitude control system for the “reimei” microsatellite. In *Advanced Motion Control, 2008. AMC’08. 10th IEEE International Workshop on*, pages 584–589. IEEE, 2008. 29
- [26] Takaya Inamori, Nobutada Sako, and Shinichi Nakasuka. Magnetic dipole moment estimation and compensation for an accurate attitude control in nano-satellite missions. *Acta Astronautica*, 68(11):2038–2046, 2011. 29
- [27] WH Steyn and Y Hashida. In-orbit attitude performance of the 3-axis stabilised snap-1 nanosatellite. *Proceedings of the AIAA/USU Conference on Small Satellites*, 2001. 29
- [28] Takaya Inamori, Shinichi Nakasuka, and Nobutada Sako. In-orbit magnetic disturbance estimation and compensation using ukf in nano-satellite mission. In *Proc. AIAA Guidance, Navigation, and Control Conference, Chicago, USA*, 2009. 29
- [29] Takayuki Hosonuma. A precise attitude determination and control strategy for small astrometry satellite “nano-jasmine”. *Proceedings of the AIAA/USU Conference on Small Satellites*, 2012. 29
- [30] S Seriani, YL Brama, P Gallina, and G Manzoni. In-orbit offline estimation of the residual magnetic dipole biases of the popsat-hip1 nanosatellite. *Acta Astronautica*, 122:10–18, 2016. 29

-
- [31] Amit Jain and Avinashi Kapoor. Exact analytical solutions of the parameters of real solar cells using lambert w-function. *Solar Energy Materials and Solar Cells*, 81(2):269–277, 2004. 32
 - [32] F Landis Markley. Unit quaternion from rotation matrix. *Journal of guidance, control, and dynamics*, 31(2):440, 2008. 39
 - [33] Stanley Wayne Shepperd. Quaternion from rotation matrix.[four-parameter representation of coordinate transformation matrix]. 1(1):223–224, 1978. 39

TRITA 2017:104
ISSN 1653-5146